The Astrophysical Journal, 901:166 (21pp), 2020 October 1 https://doi.org/10.3847/1538-4357/abb1a2

Temperature Structures of Embedded Disks: Young Disks in Taurus Are Warm

Merel L. R. van 't Hoff[1,2], Daniel Harsono[1,3], John J. Tobin[4], Arthur D. Bosman[1,2], Ewine F. van Dishoeck[1,5], Jes K. Jørgensen[6], Anna Miotello[7], Nadia M. Murillo[1,8], and Catherine Walsh[9]
[1] Leiden Observatory, Leiden University, P.O. Box 9513, 2300 RA Leiden, The Netherlands; mervth@umich.edu
[2] Department of Astronomy, University of Michigan, 1085 South University Avenue, Ann Arbor, MI 48109, USA
[3] Institute of Astronomy and Astrophysics, Academia Sinica, No. 1, Section 4, Roosevelt Road, Taipei 10617, Taiwan, R.O. C.
[4] National Radio Astronomy Observatory, 520 Edgemont Road, Charlottesville, VA 22903, USA
[5] Max-Planck-Institut für Extraterrestrische Physik, Giessenbachstrasse 1, D-85748 Garching bei München, Germany
[6] Niels Bohr Institute, University of Copenhagen, Øster Voldgade 5-7, DK-1350 Copenhagen K., Denmark
[7] European Southern Observatory, Karl-Schwarzschild-Str. 2, D-85748 Garching bei München, Germany
[8] The Institute of Physical and Chemical Research (RIKEN), 2-1, Hirosawa, Wako-shi, Saitama 351-0198, Japan
[9] School of Physics and Astronomy, University of Leeds, Leeds LS2 9JT, UK
Received 2020 July 13; revised 2020 August 17; accepted 2020 August 18; published 2020 October 6

Abstract

The chemical composition of gas and ice in disks around young stars sets the bulk composition of planets. In contrast to protoplanetary disks (Class II), young disks that are still embedded in their natal envelope (Class 0 and I) are predicted to be too warm for CO to freeze out, as has been confirmed observationally for L1527 IRS. To establish whether young disks are generally warmer than their more evolved counterparts, we observed five young (Class 0/I and I) disks in Taurus with the Atacama Large Millimeter/submillimeter Array, targeting $C^{17}O$ 2 − 1, H_2CO $3_{1,2} - 2_{1,1}$, HDO $3_{1,2} - 2_{2,1}$, and CH_3OH $5_K - 4_K$ transitions at $0\farcs48 \times 0\farcs31$ resolution. The different freeze-out temperatures of these species allow us to derive a global temperature structure. $C^{17}O$ and H_2CO are detected in all disks, with no signs of CO freeze-out in the inner ∼100 au and a CO abundance close to $\sim 10^{-4}$. The H_2CO emission originates in the surface layers of the two edge-on disks, as witnessed by the especially beautiful V-shaped emission pattern in IRAS 04302+2247. HDO and CH_3OH are not detected, with column density upper limits more than 100 times lower than for hot cores. Young disks are thus found to be warmer than more evolved protoplanetary disks around solar analogs, with no CO freeze-out (or only in the outermost part of $\gtrsim$100 au disks) or processing. However, they are not as warm as hot cores or disks around outbursting sources and therefore do not have a large gas-phase reservoir of complex molecules.

Unified Astronomy Thesaurus concepts: Protostars (1302); Protoplanetary disks (1300); Young stellar objects (1834); Astrochemistry (75)

1. Introduction

Disks around young stars provide the material from which planets form. Knowledge of their physical and chemical structure is therefore crucial for understanding planet formation and composition. The physics of protoplanetary disks has been studied in great detail, both using observations of individual objects (e.g., van Zadelhoff et al. 2001; Andrews et al. 2010; Andrews et al. 2018; Schwarz et al. 2016) and through surveys of star-forming regions (e.g., Ansdell et al. 2016, 2017; Barenfeld et al. 2016; Pascucci et al. 2016; Cox et al. 2017; Ruíz-Rodríguez et al. 2018; Cieza et al. 2019). Molecular line observations require more telescope time than continuum observations; hence, studies of the chemical structure generally target individual disks or small samples of bright disks (e.g., Dutrey et al. 1997; Thi et al. 2004; Öberg et al. 2010; Cleeves et al. 2015; Huang et al. 2017). The picture that is emerging for the global composition of Class II disks around solar analogs is that they have a large cold outer region ($T \lesssim 20$ K) where CO is frozen out in the disk midplanes (e.g., Aikawa et al. 2002; Mathews et al. 2013; Qi et al. 2013b, 2015, 2019; Dutrey et al. 2017).

However, it is now becoming clear that planet formation already starts when the disk is still embedded in its natal envelope. Grain growth has been observed in Class 0 and I sources, and even larger bodies may have formed before the envelope has fully dissipated (e.g., Jørgensen et al. 2009; Kwon et al. 2009; Miotello et al. 2014; ALMA Partnership et al. 2015; Harsono et al. 2018). Furthermore, the dust mass of Class II disks seems insufficient to form the observed exoplanet population, but Class 0 and I disks are massive enough (Manara et al. 2018; Tychoniec et al. 2020). Young embedded disks thus provide the initial conditions for planet formation, but unlike their more evolved counterparts, their structure remains poorly characterized.

A critical property is the disk temperature structure, because this governs disk evolution and composition. For example, temperature determines whether the gas is susceptible to gravitational instabilities (see, e.g., a review by Kratter & Lodato 2016), a potential mechanism to form giant planets, stellar companions, and accretion bursts (e.g., Boss 1997; Boley 2009; Vorobyov 2009; Tobin et al. 2016a). In addition, grain growth is thought to be enhanced in the region where water freezes out from the gas phase onto the dust grains, the water snowline ($T \sim 100$–150 K; e.g., Stevenson & Lunine 1988; Drążkowska & Alibert 2017; Schoonenberg & Ormel 2017).

Moreover, freeze-out of molecules as the temperature drops below their species-specific freeze-out temperature sets the global chemical composition of the disk. This sequential freeze-out causes radial gradients in molecular abundances and elemental ratios (like the C/O ratio; e.g., Öberg et al. 2011). In turn, the composition of a planet then depends on its formation location in the disk (e.g., Madhusudhan et al. 2014; Walsh et al. 2015; Ali-Dib 2017; Cridland et al. 2019). Finally,

the formation of high abundances of complex molecules starts from CO ice (e.g., Tielens & Hagen 1982; Garrod & Herbst 2006; Cuppen et al. 2009; Chuang et al. 2016), and COM formation will thus be impeded during the disk stage if the temperature is above the CO freeze-out temperature ($T \gtrsim 20$ K). Whether young disks are warm ($T \gtrsim 20$ K; i.e., warmer than the CO freeze-out temperature) or cold (i.e., have a large region where $T \lesssim 20$ K and CO is frozen out) is thus a simple but crucial question.

Keplerian disks are now detected around several Class 0 and I sources (e.g., Brinch et al. 2007; Tobin et al. 2012; Murillo et al. 2013; Yen et al. 2017), but most research has focused on disk formation, size, and kinematics (e.g., Yen et al. 2013; Harsono et al. 2014; Ohashi et al. 2014) or the chemical structure at the disk–envelope interface (e.g., Sakai et al. 2014b; Murillo et al. 2015; Oya et al. 2016). Only a few studies have examined the disk physical structure, and only for one particular disk, L1527 IRS. Tobin et al. (2013) and Aso et al. (2017) modeled the radial density profile, and van 't Hoff et al. (2018a) studied its temperature profile based on optically thick ^{13}CO and C^{18}O observations. The latter study showed the importance of disentangling disk and envelope emission and concluded that the entire L1527 disk is likely too warm for CO freeze-out, in agreement with model predictions (e.g., Harsono et al. 2015) but in contrast to observations of T Tauri disks.

Another important question with regard to the composition of planet-forming material is the CO abundance. The majority of protoplanetary disks have surprisingly weak CO emission, even when freeze-out and isotope-selective photodissociation are taken into account (e.g., Ansdell et al. 2016; Long et al. 2017; Miotello et al. 2017). Based on gas masses derived from HD line fluxes (Favre et al. 2013; Kama et al. 2016; McClure et al. 2016; Schwarz et al. 2016) and mass accretion rates (Manara et al. 2016) the low CO emission seems to be the result of significant CO depletion (up to 2 orders of magnitude below the interstellar medium (ISM) abundance of $\sim 10^{-4}$ with respect to H_2).

Several mechanisms have been discussed in the literature, either focusing on the chemical conversion of CO into less volatile species (e.g., Bergin et al. 2014; Eistrup et al. 2016; Bosman et al. 2018; Schwarz et al. 2018, 2019) or using dust growth to sequester CO ice in the disk midplane (e.g., Xu et al. 2017; Krijt et al. 2018). Observations of CO abundances in younger disks can constrain the timescale of the CO depletion process. Observations of ^{13}CO and C^{18}O toward the embedded sources TMC1A and L1527 are consistent with an ISM abundance (Harsono et al. 2018; van 't Hoff et al. 2018a). Recent work by Zhang et al. (2020) also found CO abundances consistent with the ISM abundance for three young disks in Taurus with ages up to ~1 Myr using optically thin ^{13}C^{18}O emission. Since the 2–3 Myr old disks in Lupus and Cha I show CO depletion by a factor of 10–100 (Ansdell et al. 2016), these results suggest that the CO abundance decreases by a factor of 10 within 1 Myr. On the other hand, Bergner et al. (2020) found C^{18}O abundances a factor of 10 below the ISM value in two Class I sources in Serpens.

In this paper, we present Atacama Large Millimeter/submillimeter Array (ALMA) observations of C^{17}O toward five young disks in Taurus to address the questions of whether young disks are generally too warm for CO freeze-out and whether there is significant CO processing. The temperature profile is further constrained by H_2CO observations, as this molecule freezes out around ~70 K. Although chemical models often assume a binding energy of 2050 K (e.g., Garrod & Herbst 2006; McElroy et al. 2013), laboratory experiments have found binding energies ranging between 3300 and 3700 K, depending on the ice surface (Noble et al. 2012). These latter values suggest H_2CO freeze-out temperatures between ~70 and 90 K for disk midplane densities ($\sim 10^8$–10^{10} cm^{-3}) instead of ~50 K. Experiments by Fedoseev et al. (2015) are consistent with the lower end of binding energies found by Noble et al. (2012), so we adopt a freeze-out temperature of 70 K for H_2CO. An initial analysis of these observations was presented in van 't Hoff (2019).

In addition, HDO and CH_3OH observations are used to probe the $\gtrsim$100–150 K region and determine whether complex molecules can be observed in these young disks, as shown for the disk around the outbursting young star V883 Ori (van 't Hoff et al. 2018b; Lee et al. 2019). In contrast, observing complex molecules has turned out to be very difficult in mature protoplanetary disks. So far, only CH_3CN has been detected in a sample of disks, and CH_3OH and HCOOH have been detected in TW Hya (Öberg et al. 2015; Walsh et al. 2016; Bergner et al. 2018; Favre et al. 2018; Loomis et al. 2018; Carney et al. 2019).

The observations are described in Section 2, and the resulting C^{17}O and H_2CO images are presented in Section 3. This section also describes the nondetections of HDO and CH_3OH. The temperature structure of the disks is examined in Section 4 based on the C^{17}O and H_2CO observations and radiative transfer modeling. The result that the young disks in this sample are warm with no significant CO freeze-out or processing is discussed in Section 5 and the conclusions are summarized in Section 6.

2. Observations

In order to study the temperature structure in young disks, a sample of five Class I protostars in Taurus was observed with ALMA: IRAS 04302+2247 (also known as the Butterfly star, hereafter IRAS 04302), L1489 IRS (hereafter L1489), L1527 IRS (hereafter L1527), TMC1, and TMC1A. All sources are known to have a disk, and Keplerian rotation has been established (Brinch et al. 2007; Tobin et al. 2012; Harsono et al. 2014, M. L. R. van 't Hoff et al. 2020, in preparation). The objects IRAS 04302 and L1527 are seen edge-on, which allows a direct view of the midplane, whereas L1489, TMC1, and TMC1A are moderately inclined by ~50°–60°. The source properties are listed in Table 1.

The observations were carried out on 2018 September 10 and 28 with a total on-source time of 15 minutes per source (project code 2017.1.01413.S). The observations used 47 antennas sampling baselines between 15 m and 1.4 km. The correlator setup included a 2 GHz continuum band with 488 kHz (0.6 km s^{-1}) resolution centered at 240.0 GHz and spectral windows targeting C^{17}O $2-1$, H_2CO $3_{1,2}-2_{1,1}$, HDO $3_{1,2}-2_{2,1}$, and several CH_3OH 5_K-4_K transitions. The spectral resolution was 122.1 kHz for CH_3OH and 61.0 kHz for the other lines, which corresponds to a velocity resolution of 0.15 and 0.08 km s^{-1}, respectively. The properties of the targeted lines can be found in Table A1.

Calibration was done using the ALMA pipeline and version 5.4.0 of the Common Astronomy Software Applications (CASA; McMullin et al. 2007). The phase calibrator was J0438+3004, and the bandpass and flux calibrator was J0510+1800. In addition, we performed up to three rounds of phase-only self-

Table 1
Overview of Source Properties

Source Name (IRAS)	Other Name	R.A.[a] (J2000)	Decl.[a] (J2000)	Class	T_{bol} (K)	L_{bol} ($L_\odot$)	M_* ($M_\odot$)	M_{env} ($M_\odot$)	M_{disk} ($M_\odot$)	R_{disk} (au)	i (deg)	Refs.[b]
04016+2610	L1489 IRS	04:04:43.1	+26:18:56.2	I	226	3.5	1.6	0.023	0.0071	600	66	1–4
04302+2247	Butterfly star	04:33:16.5	+22:53:20.4	I/II	202	0.34–0.92	0.5[c]	0.017	0.11	244	>76	3, 5, 9
04365+2535	TMC1A	04:39:35.2	+25:41:44.2	I	164	2.5	0.53–0.68	0.12	0.003–0.03	100	50	1, 6–8
04368+2557	L1527 IRS	04:39:53.9	+26:03:09.5	0/I	59	1.9–2.75	0.19–0.45	0.9–1.7	0.0075	75–125	85	9–14
04381+2540	TMC1	04:41:12.7	+25:46:34.8	I	171	0.66–0.9	0.54	0.14	0.0039	100	55	1, 6, 10

Notes. All values presented in this table are from the literature listed in footnote b. Here TMC1 is resolved for the first time as a binary. The literature values in this table are derived assuming a single source.
[a] Peak of the continuum emission, except for TMC1, where the phase center of the observations is listed. The coordinates of the two sources TMC1-E and TMC1-W are R.A. = 04:41:12.73, decl. = +25:46:34.76 and R.A. = 04:41:12.69, decl. = +25:46:34.73, respectively.
[b] References. (1) Green et al. (2013), (2) Yen et al. (2014), (3) Sheehan & Eisner (2017), (4) Sai et al. (2020), (5) Wolf et al. (2003), (6) Harsono et al. (2014), (7) Aso et al. (2015), (8) Harsono et al., submitted, (9) Motte & André (2001), (10) Kristensen et al. (2012), (11) Tobin et al. (2008), (12) Tobin et al. (2013), (13) Oya et al. (2015), (14) Aso et al. (2017).
[c] Not a dynamical mass.

Table 2
Observed Fluxes for the 1.3 mm Continuum and Molecular Lines

Source	F_{peak} (1.3 mm) (mJy beam^{-1})	F_{int} (1.3 mm) (mJy)	F_{int} ($C^{17}O$)[a] (Jy km s^{-1})	F_{int} (H_2CO)[a] (Jy km s^{-1})
IRAS 04302+2247	24.7 ± 0.1	165.9 ± 0.8	2.2 ± 0.2	3.5 ± 0.2
L1489 IRS	2.8 ± 0.1	51.1 ± 1.1	2.9 ± 0.3	8.0 ± 0.5
L1527 IRS	102.0 ± 0.1	195.1 ± 0.4	1.9 ± 0.4	3.0 ± 0.6
TMC1A	125.8 ± 0.2	210.4 ± 0.4	4.1 ± 0.4	2.3 ± 0.2
TMC1-E	9.2 ± 0.1	10.3 ± 0.2	2.0 ± 0.3[b]	2.6 ± 0.2[b]
TMC1-W	16.2 ± 0.1	17.6 ± 0.2	2.0 ± 0.3[b]	2.6 ± 0.2[b]

Notes. The listed errors are statistical errors and do not include calibration uncertainties.
[a] Integrated flux within a circular aperture with 6.″0 diameter.
[b] Flux for both sources together.

calibration on the continuum data with solution intervals that spanned the entire scan length for the first round, as short as 60 s in the second round, and as short as 30 s in the third round. The obtained phase solutions were also applied to the line data. Imaging was done using *tclean* in CASA version 5.6.1. The typical restoring beam size using Briggs weighting with a robust parameter of 0.5 is 0.″42 × 0.″28 (59 × 39 au) for the continuum images and 0.″48 × 0.″31 (67 × 43 au) for the line images. The continuum images have an rms of ∼0.07 mJy beam^{-1}, whereas the rms in the line images is ∼5 mJy beam^{-1} channel^{-1} for 0.08 km s^{-1} channels. The observed continuum and line flux densities are reported in Table 2.

3. Results

3.1. $C^{17}O$ and H_2CO Morphology

Figure 1 shows the 1.3 mm continuum images and integrated intensity (zeroth moment) maps for $C^{17}O$ 2 − 1 and H_2CO $3_{1,2} - 2_{1,1}$ toward the five sources in our sample. The molecular emission toward IRAS 04302 is highlighted at slightly higher spatial resolution in Figure 2. Radial cuts along the major axis are presented in Figure 3. The continuum emission is elongated perpendicular to the outflow direction for all sources, consistent with a disk as observed before. For the first time, TMC1 is resolved into a close binary (∼85 au separation). We will refer to the two sources as TMC1-E (east) and TMC1-W (west).

Both $C^{17}O$ and H_2CO are clearly detected toward all sources with a velocity gradient along the continuum structures (see Figure A1). The velocity gradient suggests that the material in TMC1 is located in a circumbinary disk, but a detailed analysis is beyond the scope of this paper. For both molecules, integrated fluxes are similar (within a factor of 2–3) in all sources (Table 2), and both lines have a comparable (factor of 2–4) strength toward each source, with H_2CO brighter than $C^{17}O$, except for TMC1A. The H_2CO emission is generally more extended than the $C^{17}O$ emission, both radially and vertically, except toward TMC1 and TMC1A, where both molecules have the same spatial extent. This is not a signal-to-noise issue, as can be seen from the radial cuts along the major axis (Figure 3).

The most striking feature in the integrated intensity maps is the V-shaped emission pattern of the H_2CO in the edge-on disk IRAS 04302 (see Figure 2), suggesting that the emission arises from the disk surface layers and not the midplane, in contrast to the $C^{17}O$ emission. The H_2CO emission displays a ringlike structure toward L1527. Given that this disk is also viewed edge-on, this can be explained by emission originating in the disk surface layers, with the outer component along the midplane arising from the envelope. As we will show later in this section, the emission toward IRAS 04302 shows very little envelope contribution, which can explain the difference in morphology between these two sources. The $C^{17}O$ emission peaks slightly offset (∼60 au) from the L1527 continuum peak, probably due to the dust becoming optically thick in the inner ∼10 au, as seen before for ^{13}CO and $C^{18}O$ (van 't Hoff et al. 2018a). The current resolution does not resolve the inner 10 au; hence, the reduction in CO emission is more extended. In IRAS 04302, a similar offset of

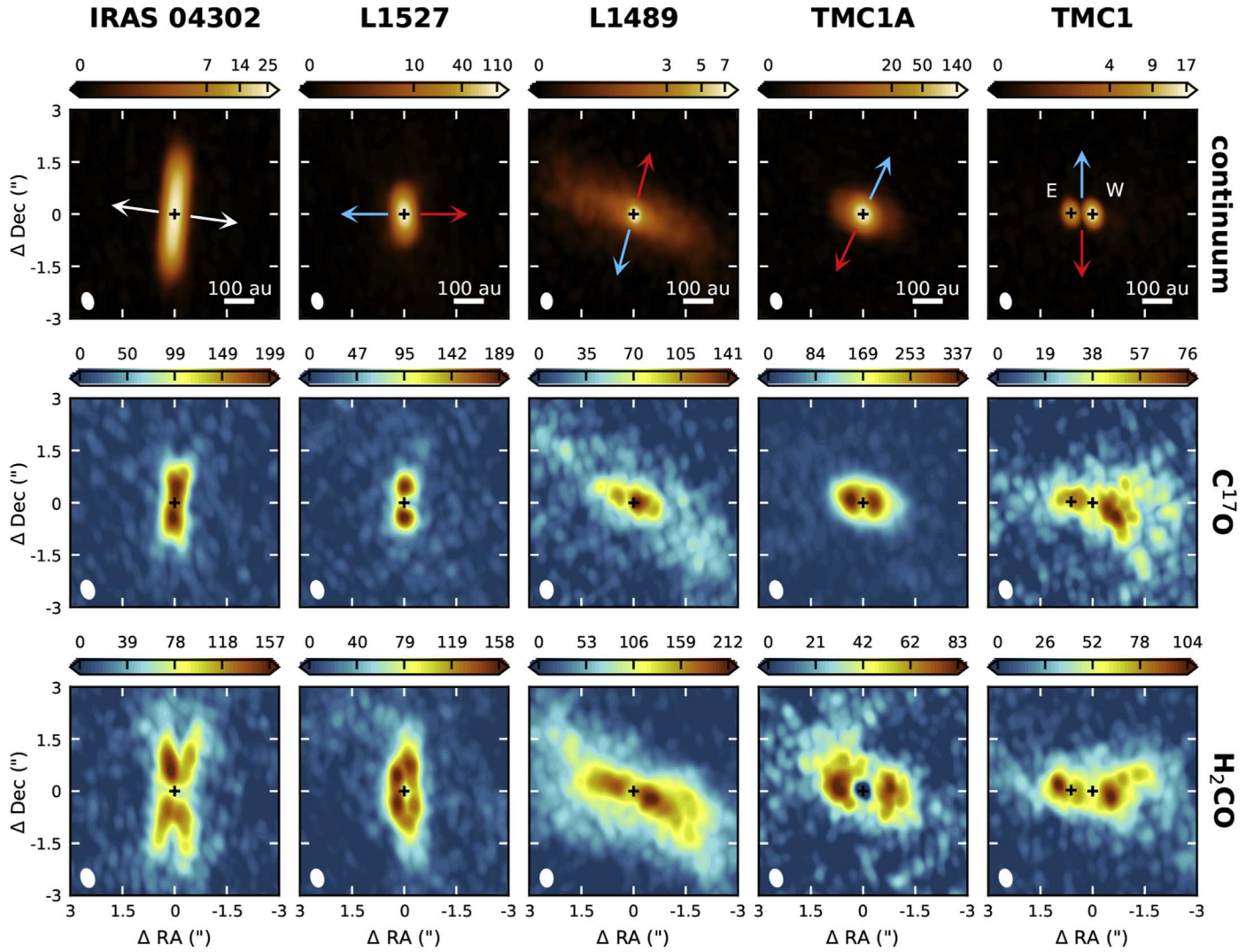

Figure 1. Continuum images at 1.3 mm (top row) and integrated intensity maps for the $C^{17}O$ 2 − 1 (middle row) and H_2CO $3_{1,2} - 2_{1,1}$ (bottom row) transitions. The color scale is in mJy beam^{-1} for the continuum images and mJy beam^{-1} km s^{-1} for the line images. The positions of the continuum peaks are marked with black plus signs, and the outflow directions are indicated by arrows in the continuum images. The beam is shown in the lower left corner of each panel.

∼60 au is found for both $C^{17}O$ and H_2CO, suggesting that there may be an unresolved optically thick dust component as well.

Toward L1489, $C^{17}O$ has a bright inner component (∼200 au) and a weaker outer component that extends roughly as far as the H_2CO emission (∼600 au). A similar structure was observed in $C^{18}O$ by Sai et al. (2020). The slight rise seen in $C^{18}O$ emission around ∼300 au to the southwest of the continuum peak is also visible in the $C^{17}O$ radial cut. Imaging the $C^{17}O$ data at lower resolution makes this feature clearer in the integrated intensity map. In contrast, the H_2CO emission decreases in the inner ∼75 au, but beyond that, it extends smoothly out to ∼600 au. The off-axis protrusions at the outer edge of the disk pointing to the northeast and southwest were also observed in $C^{18}O$ and explained as streams of infalling material (Yen et al. 2014).

The $C^{17}O$ emission peaks slightly (∼40–50 au) off source toward TMC1A. Harsono et al. (2018) showed that ^{13}CO and $C^{18}O$ emission is absent in the inner ∼15 au due to the dust being optically thick. The resolution of the $C^{17}O$ observations is not high enough to resolve this region, resulting in only a central decrease in emission instead of a gap. A clear gap is visible for H_2CO with the emission peaking ∼100–115 au off source. The central absorption falling below zero is an effect of resolved-out large-scale emission.

Finally, toward TMC1, H_2CO shows a dip at both continuum peaks, while the $C^{17}O$ emission is not affected by the eastern continuum peak. As discussed for the other sources, this may be the result of optically thick dust in the inner disk. The protrusions seen on the west side in both $C^{17}O$ and H_2CO are part of a larger arc-like structure that extends toward the southwest beyond the scale shown in the image.

While it is tempting to ascribe all of the compact emission to the young disk, some of it may also come from the envelope and obscure the disk emission. To get a first impression as to whether the observed emission originates in the disk or envelope, position–velocity (*pv*) diagrams are constructed along the disk major axis for the four single sources (Figure 4). In these diagrams, disk emission is located at small angular offsets and high velocities, while envelope emission extends to larger offsets but has lower velocities. In all sources, $C^{17}O$ predominantly traces the disk, with some envelope contribution, especially in L1527 and L1489. The H_2CO emission also originates in the disk but has a larger envelope component. An exception is IRAS 04302, which shows hardly

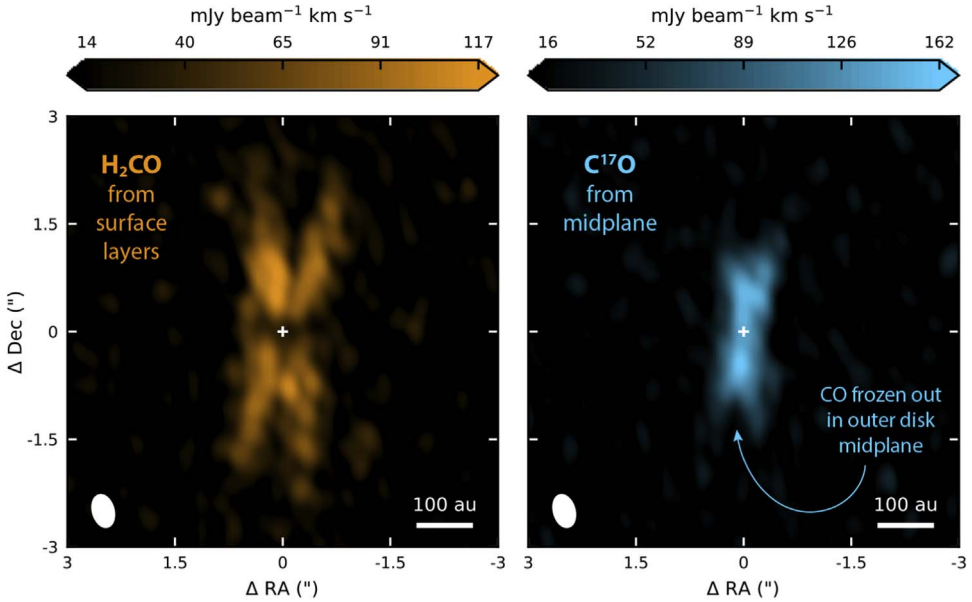

Figure 2. Integrated intensity maps for the H_2CO $3_{1,2} - 2_{1,1}$ (left) and $C^{17}O$ $2 - 1$ (right) emission toward IRAS 04302. These images have slightly higher resolution than shown in Figure 1 ($0\farcs45 \times 0\farcs28$) due to uniform weighting of the visibilities. The positions of the continuum peaks are marked with white plus signs, and the beam is shown in the lower left corner of each panel.

any envelope contribution. These results for L1527 are in agreement with previous observations (Sakai et al. 2014a). In L1489, a bright linear feature is present for H_2CO extending from a velocity and angular offset of $-2\,\mathrm{km\,s^{-1}}$ and $-2''$, respectively, to offsets of $2\,\mathrm{km\,s^{-1}}$ and $2''$. This feature matches the shape of the SO *pv* diagram (Yen et al. 2014), which was interpreted by the authors as a ring between ~250 and 390 au. While a brightness enhancement was also identified by Yen et al. (2014) in the $C^{18}O$ emission (similar to that seen here for H_2CO), the $C^{17}O$ emission does not display such a feature.

Another way to determine the envelope contribution is from the visibility amplitudes. Although a quantitative limit on the envelope contribution to the line emission requires detailed modeling for the individual sources, which will be done in a subsequent paper, a first assessment can be made with more generic models containing either only a Keplerian disk or a disk embedded in an envelope (see Appendix B). For IRAS 04302, both the $C^{17}O$ and H_2CO visibility amplitude profiles can be reproduced without an envelope. This suggests that there is very little envelope contribution for this source, consistent with the *pv* diagrams. A disk is also sufficient to reproduce the visibility amplitudes at velocities $>|1|\,\mathrm{km\,s^{-1}}$ from the systemic velocity toward L1489, L1527, and TMC1A. For the low velocities, a small envelope contribution is required. The line emission presented here is thus dominated by the disk.

Although both the $C^{17}O$ and H_2CO emission originates predominantly from the disk, the $C^{17}O$ emission extends to higher velocities than the H_2CO emission in IRAS 04302, L1527, and TMC1A. This is more easily visualized in the spectra presented in Figure A2. These spectra are extracted in a $6''$ circular aperture and only include pixels with $>3\sigma$ emission. While H_2CO is brighter at intermediate velocities than $C^{17}O$ (even when correcting for differences in emitting area), it is not present at the highest velocities. Thus, H_2CO emission seems to be absent in the inner disk in these sources, which for TMC1A is also visible in the moment zero map (Figure 1). However, in L1489, both molecules have similar maximum velocities. Toward TMC1, they extend to the same redshifted velocity, while $C^{17}O$ emission is strongly decreased at blueshifted velocities as compared to the redshifted velocities.

3.2. $C^{17}O$ and H_2CO Column Densities and Abundances

To compare the $C^{17}O$ and H_2CO observations between the different sources more quantitatively, we calculate disk-averaged total column densities, N_T, assuming optically thin emission in local thermodynamic equilibrium (LTE) using

$$\frac{4\pi F\Delta v}{A_{ul}\Omega hcg_{\rm up}} = \frac{N_T}{Q(T_{\rm rot})}e^{-E_{\rm up}/kT_{\rm rot}}, \quad (1)$$

where $F\Delta v$ is the integrated flux density; A_{ul} is the Einstein A coefficient; Ω is the solid angle subtended by the source; $E_{\rm up}$ and $g_{\rm up}$ are the upper-level energy and degeneracy, respectively; and $T_{\rm rot}$ is the rotational temperature.

The integrated fluxes are measured over the dust-emitting area (Table 3). We note that this does not necessarily encompass the total line flux, but it will allow for an abundance estimate as described below. A temperature of 30 K is adopted for $C^{17}O$ and 100 K for H_2CO, as these are slightly above their freeze-out temperatures. The $C^{17}O$ column density ranges between ~2 and $20 \times 10^{15}\,\mathrm{cm^{-2}}$, with the lowest value toward L1489 and the highest value toward TMC1A. The H_2CO column density is about an order of magnitude lower, with values between ~4 and $18 \times 10^{14}\,\mathrm{cm^{-2}}$. The lowest value is found toward TMC1A, and the highest value is found toward L1527. Changing the temperature for H_2CO to 30 K decreases the column densities by only a factor of $\lesssim$3.

The H_2CO column density toward L1527 is a factor of 3–6 higher than previously derived by Sakai et al. (2014a), possibly because they integrated over different areas and velocity ranges for the envelope, disk, and envelope–disk interface. Integrating the H_2CO emission over a circular aperture of $0\farcs5$ and excluding the central $|\Delta v| \leqslant 1.0\,\mathrm{km\,s^{-1}}$ channels to limit the contribution from the envelope and resolved-out emission results in an H_2CO column density of $9.7 \times 10^{13}\,\mathrm{cm^{-2}}$, only a factor of 2–3 higher than that found by Sakai et al. (2014a).

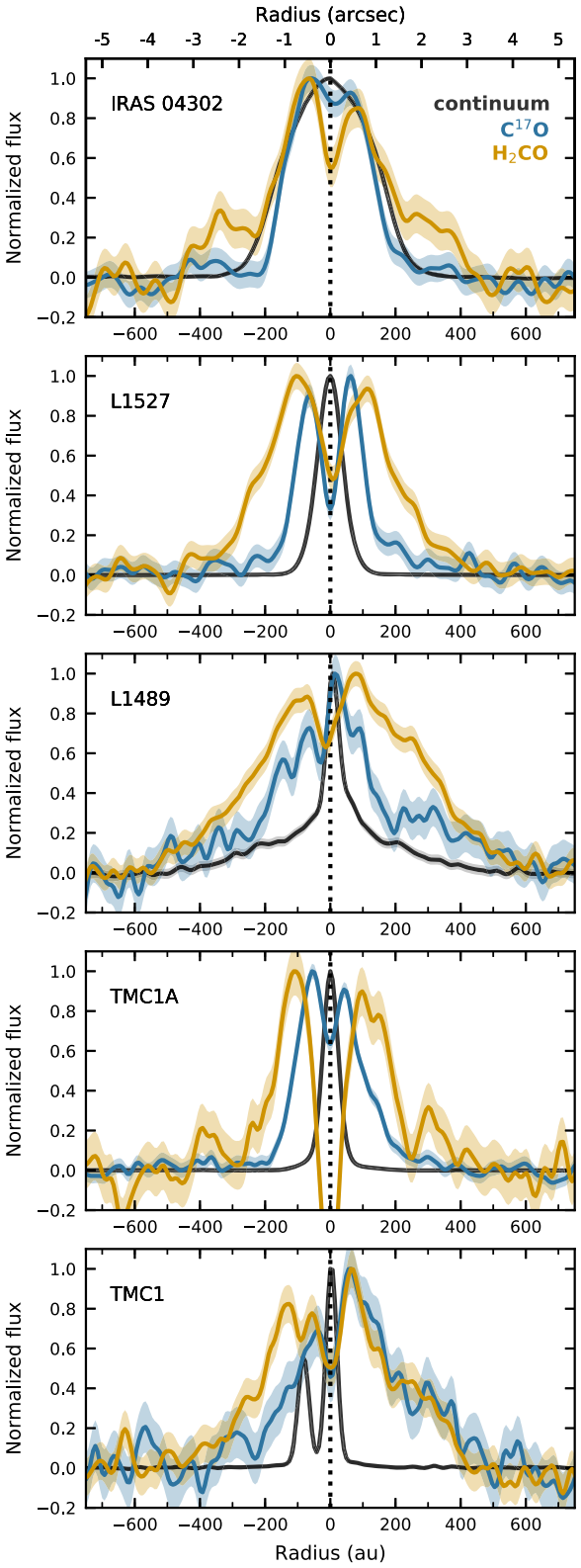

Figure 3. Normalized radial cuts along the disk major axis for the 1.3 mm continuum flux (black) and the $C^{17}O$ (blue) and H_2CO (orange) integrated intensities. The shaded area shows the 3σ uncertainty.

Pegues et al. (2020) found H_2CO column densities spanning 3 orders of magnitude ($\sim 5 \times 10^{11}$–5×10^{14} cm^{-2}) for a sample of 13 Class II disks. The values derived here for Class I disks are thus similar to the high end ($\lesssim$4 times higher) of the values for Class II disks.

An assessment of the molecular abundances can be made by estimating the H_2 column density from the continuum flux. First, we calculate the disk dust masses, $M_{\rm dust}$, from the integrated continuum fluxes, F_ν, using

$$M_{\rm dust} = \frac{D^2 F_\nu}{\kappa_\nu B_\nu(T_{\rm dust})}, \quad (2)$$

where D is the distance to the source, κ_ν is the dust opacity with the assumption of optically thin emission, and B_ν is the Planck function for a temperature $T_{\rm dust}$ (Hildebrand 1983). Adopting a dust opacity of $\kappa_{1.3\rm mm} = 2.25$ cm^2 g^{-1}, as used for Class II disks by, e.g., Ansdell et al. (2016), and a dust temperature of 30 K similar to, e.g., Tobin et al. (2015) for embedded disks results in disk dust masses between 3.7 M_E for TMC1-E and 75 M_E for TMC1A. Using the same dust opacity as for Class II disks is probably reasonable if grain growth starts early on in the disk formation process. However, adopting $\kappa_{1.3\rm mm} = 0.899$ cm^2 g^{-1}, as is often done for protostellar disks and envelopes (e.g., Jørgensen et al. 2007; Andersen et al. 2019; Tobin et al. 2020), only affects the molecular abundances by a factor of $\sim$2. Assuming a gas-to-dust ratio of 100 and using the size of the emitting region, these dust masses result in H_2 column densities of 2–90 $\times$ 10^{23} cm^{-2}.

The resulting $C^{17}O$ and H_2CO abundances are listed in Table 3. For $C^{17}O$, the abundances range between 1.2×10^{-8} and 1.2×10^{-7}. Assuming a $C^{16}O/C^{17}O$ ratio of 1792 (as in the ISM; Wilson & Rood 1994), a CO ISM abundance of 10^{-4} with respect to H_2 corresponds to a $C^{17}O$ abundance of 5.6×10^{-8}. The derived $C^{17}O$ abundances are thus within a factor of 5 of the ISM abundance, suggesting that no substantial processing has happened, as observed for Class II disks where the CO abundance can be 2 orders of magnitude below the ISM value (e.g., Favre et al. 2013). These results are consistent with the results from Zhang et al. (2020) for three Class I disks in Taurus (including TMC1A) but not with the order-of-magnitude depletion found by Bergner et al. (2020) for two Class I disks in Serpens. For H_2CO, the abundance ranges between $\sim 3 \times 10^{-10}$ and $\sim 8 \times 10^{-9}$ in the different sources, except for TMC1A, where the abundance is $\sim 5 \times 10^{-11}$, probably due to the absence of emission in the inner region. Abundances around 10^{-10}–10^{-9} are consistent with chemical models for protoplanetary disks (e.g., Willacy & Woods 2009; Walsh et al. 2014). However, H_2CO abundances derived for TW Hya and HD 163296 are 2–3 orders of magnitude lower, 8.9×10^{-13} and 6.3×10^{-12}, respectively (Carney et al. 2019).

A caveat in determining these abundances is the assumption that the continuum and line emission are optically thin. As discussed in Section 3.1, there is likely an optically thick dust component that would result in underestimates of the dust masses and overestimates of the abundances. On the other hand, optically thick dust hides molecular line emission originating below its $\tau = 1$ surface, which leads to underestimates of the abundances. Based on the results from Zhang et al. (2020), $C^{17}O$ may be optically thick in Class I disks. This would also result in underestimating the abundances. Scaling the dust temperature used in Equation (2) with luminosity, as done by Tobin et al. (2020) for embedded disks in Orion, results in dust masses lower by a factor of $\sim$2 and therefore slightly higher abundances. Moreover, the integrated line flux is assumed to originate solely in the disk, but as shown in Figure 4, there can be envelope emission present. Finally, the H_2CO emission originates in the disk surface layers, which

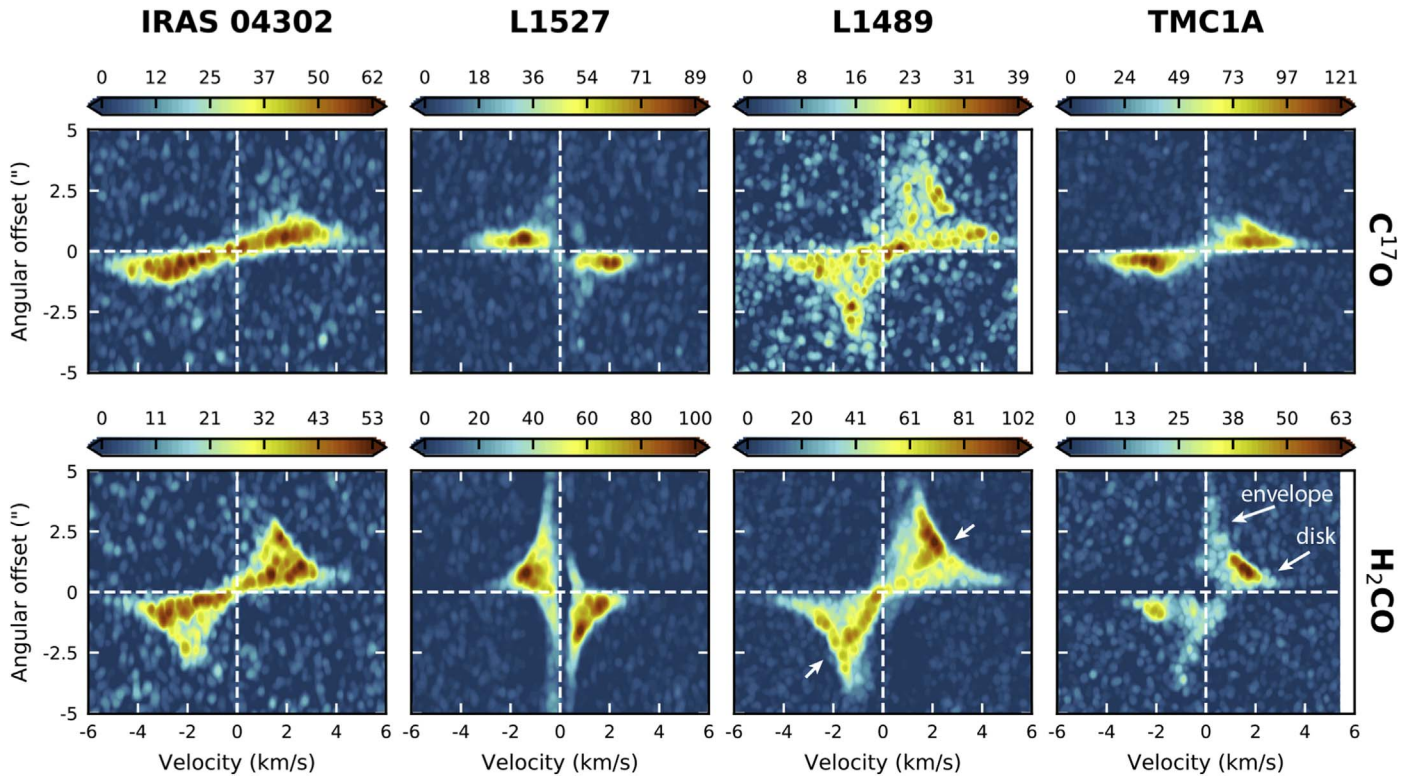

Figure 4. The *pv* diagrams for $C^{17}O$ (top panels) and H_2CO (bottom panels) along the major axis of the disks in the single systems (listed above the rows). $C^{17}O$ predominantly traces the disk, that is, high velocities at small angular offsets, whereas H_2CO generally has a larger envelope component, that is, low velocities at large angular offsets. The velocity is shifted such that 0 km s^{-1} corresponds to the systemic velocity. The color scale is in mJy $beam^{-1}$. The white arrows in the L1489 H_2CO panel highlight the linear feature that is described in the text.

means the abundances are higher than derived here assuming emission originating throughout the disk. To take all these effects into account, source-specific models are required.

3.3. HDO and CH_3OH Upper Limits

Water and methanol form on ice-covered dust grains and thermally desorb into the gas phase at temperatures ∼100–150 K. These molecules are thus expected to trace the hot region inside the water snowline. The observations cover one HDO (deuterated water) transition ($3_{1,2} - 2_{2,1}$) with an upper-level energy of 168 K and 16 transitions in the CH_3OH $J = 5_k - 4_k$ branch with upper-level energies ranging between 34 and 131 K. None of these lines are detected in any of the disks.

To compare these nondetections to observations in other systems, a 3σ upper limit is calculated for the disk-averaged total column density by substituting

$$3\sigma = 3 \times 1.1\sqrt{\delta v \Delta V} \times \mathrm{rms} \quad (3)$$

for the integrated flux density, $F\Delta v$, in Equation (1). Here δv is the velocity resolution, and ΔV is the line width expected based on other line detections. The factor of 1.1 takes a 10% calibration uncertainty into account. Assuming the water and methanol emission arises from the innermost part of the disk, the rms is calculated from the baseline of the spectrum integrated over a central 0.″5 diameter aperture (∼one beam) and amounts to ∼2.7 mJy for HDO and ∼3.0 mJy for CH_3OH. A line width of 4 km s^{-1} and a rotational temperature of 100 K are adopted.

A 3σ column density upper limit of $\sim 8 \times 10^{13}$ cm^{-2} is then found for HDO. This is 1–2 orders of magnitude below the column densities derived for the Class 0 sources NGC1333 IRAS2A, NGC1333 IRAS4A-NW, and NGC1333 IRAS4B ($\sim 10^{15}$–10^{16} cm^{-2}; Persson et al. 2014) and more than 3 orders of magnitude lower than toward the Class 0 source IRAS 16293A ($\sim 5 \times 10^{17}$ cm^{-2}; Persson et al. 2013). Taking into account the larger beam size of the earlier observations (∼1″) lowers the column density derived here by only a factor of ∼4. Furthermore, Taquet et al. (2013) showed that the HDO observations toward NGC1333 IRAS2A and NGC1333 IRAS4A are consistent with column densities up to 10^{19} and 10^{18} cm^{-2}, respectively, using a grid of non-LTE large velocity gradient (LVG) radiative transfer models.

For CH_3OH, the $5_{0,5} - 4_{0,4}$ (A) transition provides the most stringent upper limit of $\sim 8 \times 10^{14}$ cm^{-2}. This upper limit is orders of magnitude lower than the column density toward the Class 0 source IRAS 16293 (2×10^{19} cm^{-2} within a 70 au beam; Jørgensen et al. 2016) and the young disk around the outbursting star V883 Ori (disk-averaged column density of $\sim 1.0 \times 10^{17}$ cm^{-2}; van 't Hoff et al. 2018b). A similarly low upper limit (5×10^{14} cm^{-2}) was found for a sample of 12 Class I disks in Ophiuchus (Artur de la Villarmois et al. 2019). However, this upper limit is not stringent enough to constrain the column down to the value observed in the TW Hya protoplanetary disk (peak column density of 3–6 $\times 10^{12}$ cm^{-2}; Walsh et al. 2016) or the upper limit in the Herbig Ae disk HD 163296 (disk-averaged upper limit of 5×10^{11} cm^{-2}; Carney et al. 2019).

For a better comparison with other sources, column density ratios are calculated with respect to H_2 and H_2CO and reported in Table 3. Using the H_2 column density derived from the continuum flux, upper limits of ~ 1–40×10^{-10} are found for the HDO abundance. The CH_3OH upper limits range between 1 and 40×10^{-9}. This is orders of magnitude lower than what is

Table 3
Column Densities and Column Density Ratios

Source	Molecule	Area[a] (arcsec × arcsec)	F_{int}[b] (Jy km s^{-1})	N[c] (cm^{-2})	$N/N(H_2)$[d]	$N/N(H_2CO)$[e]
IRAS 04302	$C^{17}O$	3.95 × 1.01	1.4 ± 0.05	5.5 ± 0.41 × 10^{15}	3.8 × 10^{-8}	46
	H_2CO	3.95 × 1.01	1.5 ± 0.05	1.2 ± 0.04 × 10^{14}	8.4 × 10^{-10}	⋯
	HDO	0.50 × 0.50	<4.5 × 10^{-3}	<7.4 × 10^{13}	<5.3 × 10^{-10}	<0.62
	CH_3OH	0.50 × 0.50	<6.9 × 10^{-3}	<7.3 × 10^{14}	<5.2 × 10^{-9}	<6.1
L1489	$C^{17}O$	4.05 × 2.19	1.5 ± 0.11	2.3 ± 0.40 × 10^{15}	1.2 × 10^{-7}	15
	H_2CO	4.05 × 2.19	4.2 ± 0.11	1.5 ± 0.04 × 10^{14}	7.6 × 10^{-9}	⋯
	HDO	0.50 × 0.50	<5.0 × 10^{-3}	<8.3 × 10^{13}	<4.2 × 10^{-9}	<0.55
	CH_3OH	0.50 × 0.50	<8.4 × 10^{-3}	<8.8 × 10^{14}	<4.4 × 10^{-8}	<5.9
L1527	$C^{17}O$	1.34 × 0.77	0.54 ± 0.03	7.7 ± 0.96 × 10^{15}	1.2 × 10^{-8}	43
	H_2CO	1.34 × 0.77	0.55 ± 0.03	1.8 ± 0.10 × 10^{14}	2.7 × 10^{-10}	⋯
	HDO	0.50 × 0.50	<5.6 × 10^{-3}	<9.2 × 10^{13}	<1.4 × 10^{-10}	<0.51
	CH_3OH	0.50 × 0.50	<7.9 × 10^{-3}	<8.3 × 10^{14}	<1.3 × 10^{-9}	<4.6
TMC1A	$C^{17}O$	0.93 × 0.88	1.1 ± 0.02	2.0 ± 0.08 × 10^{16}	2.3 × 10^{-8}	488
	H_2CO	0.93 × 0.88	0.10 ± 0.02	4.1 ± 0.82 × 10^{13}	4.6 × 10^{-11}	⋯
	HDO	0.50 × 0.50	<5.0 × 10^{-3}	<8.3 × 10^{13}	<9.3 × 10^{-11}	<2.0
	CH_3OH	0.50 × 0.50	<7.7 × 10^{-3}	<8.1 × 10^{14}	<9.1 × 10^{-10}	<18
TMC1-E	$C^{17}O$	0.71 × 0.54	0.10 ± 0.01	3.6 ± 0.85 × 10^{15}	3.9 × 10^{-8}	33
	H_2CO	0.71 × 0.54	0.12 ± 0.01	1.1 ± 0.09 × 10^{14}	1.2 × 10^{-9}	⋯
	HDO	0.50 × 0.50	<5.0 × 10^{-3}	<8.3 × 10^{13}	<8.9 × 10^{-10}	<0.75
	CH_3OH	0.50 × 0.50	<7.7 × 10^{-3}	<8.1 × 10^{14}	<8.7 × 10^{-9}	<7.4
TMC1-W	$C^{17}O$	0.81 × 0.63	0.12 ± 0.01	3.3 ± 0.65 × 10^{15}	2.8 × 10^{-8}	35
	H_2CO	0.81 × 0.63	0.15 ± 0.01	9.5 ± 0.66 × 10^{13}	8.0 × 10^{-9}	⋯
	HDO	0.50 × 0.50	<5.0 × 10^{-3}	<8.3 × 10^{13}	<6.9 × 10^{-10}	<0.87
	CH_3OH	0.50 × 0.50	<7.7 × 10^{-3}	<8.1 × 10^{14}	<6.8 × 10^{-9}	<8.5

Notes.
[a] Area over which the flux is extracted.
[b] Integrated flux. For HDO and CH_3OH, this is the 3σ upper limit to the integrated flux.
[c] Column density.
[d] Column density with respect to H_2, where the H_2 column density is estimated from the continuum flux and assuming a gas-to-dust ratio of 100.
[e] Column density with respect to H_2CO.

expected from ice observations ($10^{-6} - 10^{-5}$; Boogert et al. 2015), and thus from thermal desorption, as observed in IRAS 16293 ($\lesssim 3 \times 10^{-6}$; Jørgensen et al. 2016) and V883 Ori ($\sim 4 \times 10^{-7}$; van 't Hoff et al. 2018b). Abundances for nonthermally desorbed CH_3OH in TW Hya are estimated to be $\sim 10^{-12} - 10^{-11}$ (Walsh et al. 2016). Sakai et al. (2014a) detected faint CH_3OH emission (from different transitions than targeted here) toward L1527, with a CH_3OH/H_2CO ratio between 0.6 and 5.1. Our upper limit of 4.6 for L1527 is consistent with these values. CH_3OH/H_2CO ratios of 1.3 and <0.2 were derived for TW Hya and HD 163296, respectively, but our CH_3OH upper limit is not stringent enough to make a meaningful comparison. An assumption here is that the emitting regions of CH_3OH and H_2CO are cospatial. As noted in Section 3.1, H_2CO seems absent in the inner disk where CH_2OH is expected.

4. Analysis

4.1. Temperature Structure in Edge-on Disks

For (near) edge-on disks, CO freeze-out should be readily observable, as CO emission will be missing from the outer disk midplane (Dutrey et al. 2017; van 't Hoff et al. 2018a). Van 't Hoff et al. (2018a) studied the effect of CO freeze-out on the optically thick ^{13}CO and $C^{18}O$ emission in L1527. The less abundant $C^{17}O$ is expected to be optically thin and mainly traces the disk. Here we employ the models from van 't Hoff et al. (2018a) to predict the $C^{17}O$ emission pattern for varying degrees of CO freeze-out (see Figure C1): a "warm" model (no CO freeze-out), an "intermediate" model (CO freeze-out in the outer disk midplane), and a "cold" model (CO freeze-out in most of the disk, except the inner part and surface layers). Briefly, in these models, gaseous CO is present at a constant abundance of 10^{-4} with respect to H_2 in the regions in the disk where $T > 20$ K and in the envelope. For the warm model, the L1527 temperature structure from Tobin et al. (2013) is adopted, and for the intermediate and cold models, the temperature is reduced by 40% and 60%, respectively. There is no CO freeze-out in the 125 au disk in the warm model, while the intermediate and cold models have the CO snowline at 71 and 23 au, respectively. Synthetic image cubes are generated using the radiative transfer code LIME (Brinch & Hogerheijde 2010), making use of the $C^{17}O$ LAMDA file (Schöier et al. 2005) for the LTE calculation, and are convolved with the observed beam size.

Figure 5 shows moment zero maps integrated over the low, intermediate, and high velocities for the warm and cold edge-on disk model. Models with and without an envelope are presented. The difference between the warm and cold model is most clearly distinguishable at intermediate velocities (Figure 5, middle row). In the absence of an envelope, the emission becomes V-shaped in the cold model, tracing the warm surface layers where CO is not frozen out. This V shape is not visible when there is a significant envelope contribution. The cold model differs from the warm model in that the envelope emission becomes comparable in strength to the disk emission when CO is frozen out in most of the disk. In the warm case, the disk emission dominates over the envelope emission. At low velocities (Figure 5, top row), the

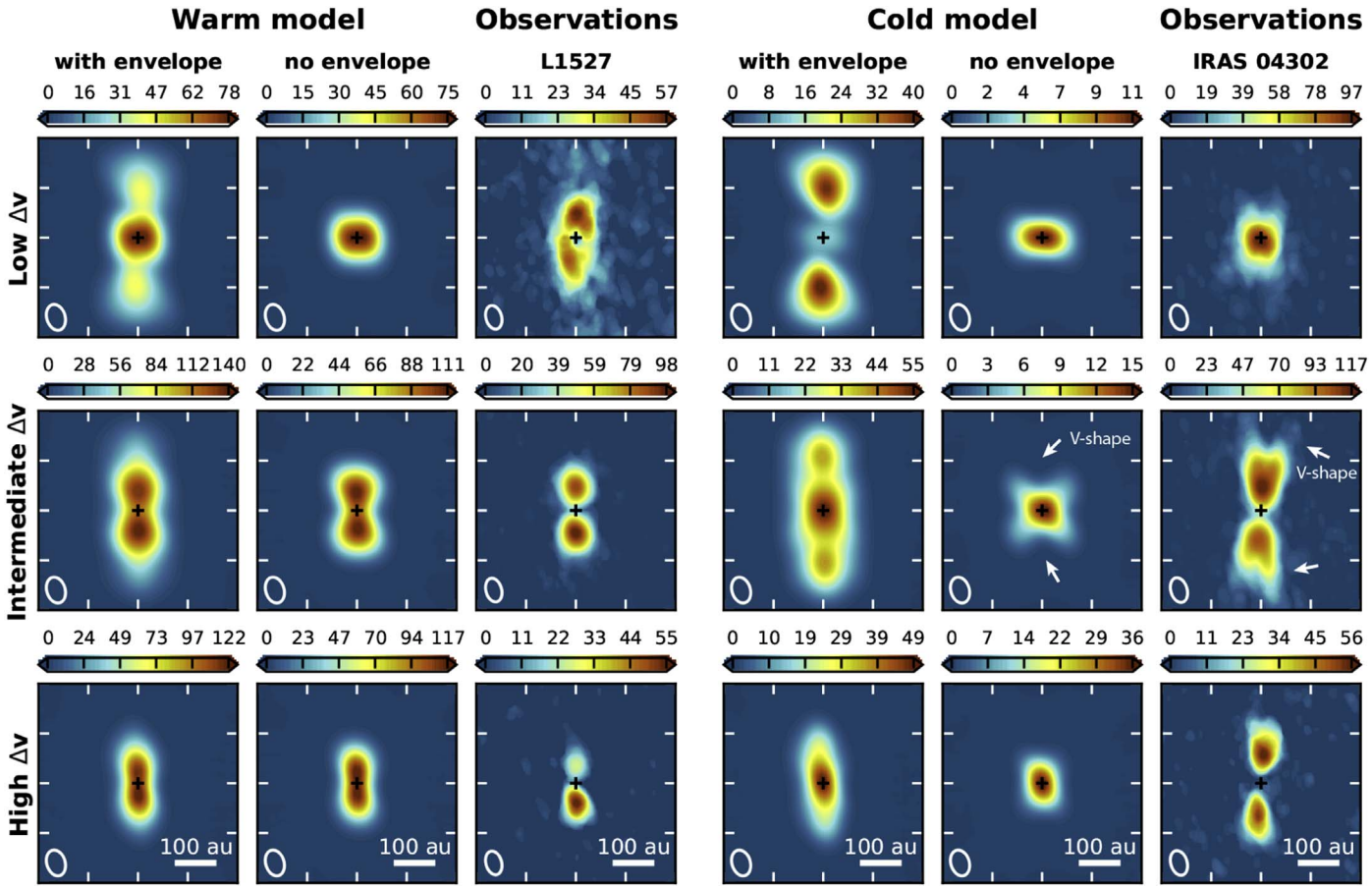

Figure 5. Integrated intensity (moment zero) maps of the low- (top row), intermediate- (middle row), and high- (bottom row) velocity $C^{17}O$ emission in the warm (first and second columns) and cold (fourth and fifth columns) edge-on disk models, as well as for the observations toward L1527 (third column) and IRAS 04302 (sixth column). The models contain either a disk and envelope (first and fourth columns) or only a disk (second and fifth columns). For the models, low velocities range from −1.0 to 1.0 km s^{-1}; intermediate velocities are $|\Delta v| = 1.0$–2.0 km s^{-1} and high velocities are $|\Delta v| = 2.0$–4.0 km s^{-1} with respect to the source velocity. For IRAS 04302 (L1527), low velocities range from −1.19 to 1.09 (−1.19 to 1.25) km s^{-1}, intermediate velocities range from −3.56 to −1.19 (−2.42 to −1.19) km s^{-1} and 1.09 to 2.97 (1.25 to 2.39) km s^{-1}, and high velocities range from −3.56 to −5.28 (−2.42 to −3.97) km s^{-1} and 2.97 to 4.67 (2.39 to 3.13) km s^{-1} with respect to the source velocity. Only pixels with $>3\sigma$ emission are included. The color scale is in mJy $beam^{-1}$ km s^{-1}. The source position is marked with a black plus sign, and the beam is shown in the lower left corner of the panels. A 100 au scale bar is present in the bottom panels. The V-shaped emission pattern that is visible at intermediate velocities in the cold model and the IRAS 04302 observations is indicated by white arrows.

difference between a warm and cold disk can be distinguished as well when an envelope is present, although in practice, this will be much harder due to resolved-out emission at these central velocities. Without an envelope, the low-velocity emission originates near the source center due to the rotation, and the models are indistinguishable, except for differences in the flux. Due to the rotation, the emission at these velocities gets projected along the minor axis of the disk (that is, east–west). At the highest velocities (Figure 5, top row), the emission originates in the inner disk, north and south of the source. If CO is absent in the midplane, very high angular resolution is required to observe this directly through a V-shaped pattern.

The $C^{17}O$ moment zero maps integrated over different velocity intervals for IRAS 04302 and L1527 are presented in Figure 5. The observations show no sign of CO freeze-out in L1527 and resemble the warm model (most clearly seen at intermediate velocities), consistent with previous results for $C^{18}O$ and ^{13}CO (van 't Hoff et al. 2018a). On the other hand, IRAS 04302 displays a distinct V-shaped pattern at intermediate velocities, suggesting that CO is frozen out in the outer part of this much larger disk (∼250 au, compared to 75–125 au for L1527; Tobin et al. 2013; Aso et al. 2017; Sheehan & Eisner 2017).

The vertical distribution of the emission in both disks is highlighted in Figure 6 with vertical cuts at different radii. In L1527, the $C^{17}O$ emission peaks at the midplane throughout the disk, while for IRAS 04302, the peaks shift to layers higher up in the disk for radii $\gtrsim$110 au. A first estimate of the CO snowline location can be made based on the location of the V shape. In the cold model, the CO snowline is located at 23 au, but due to the size of the beam, the base of the V shape and the first occurrence of a double peak in the vertical cuts are at ∼55 au. In IRAS 04302, the V shape begins at a radius of ∼130 au, so the CO snowline location is then estimated to be around ∼100 au.

A clear V-shaped pattern is also visible in the H_2CO integrated emission map for IRAS 04302 (Figure 1). The V shape starts at around 55 au (∼1 beam offset from the continuum peak). If the reduction of H_2CO in the midplane is fully due to freeze-out, the snowline is then located around (or inward of) ∼25 au. In L1527, H_2CO emission also appears to come from surface layers, except in the outer disk (see Figures 1 and 6). The cold models show that CO emission from the envelope becomes comparable in strength to emission from the disk if CO is frozen out in a large part of the disk. Given that the envelope contribution is much larger in L1527 than in IRAS 04302, the emission peaking in the outer disk midplane is likely originating

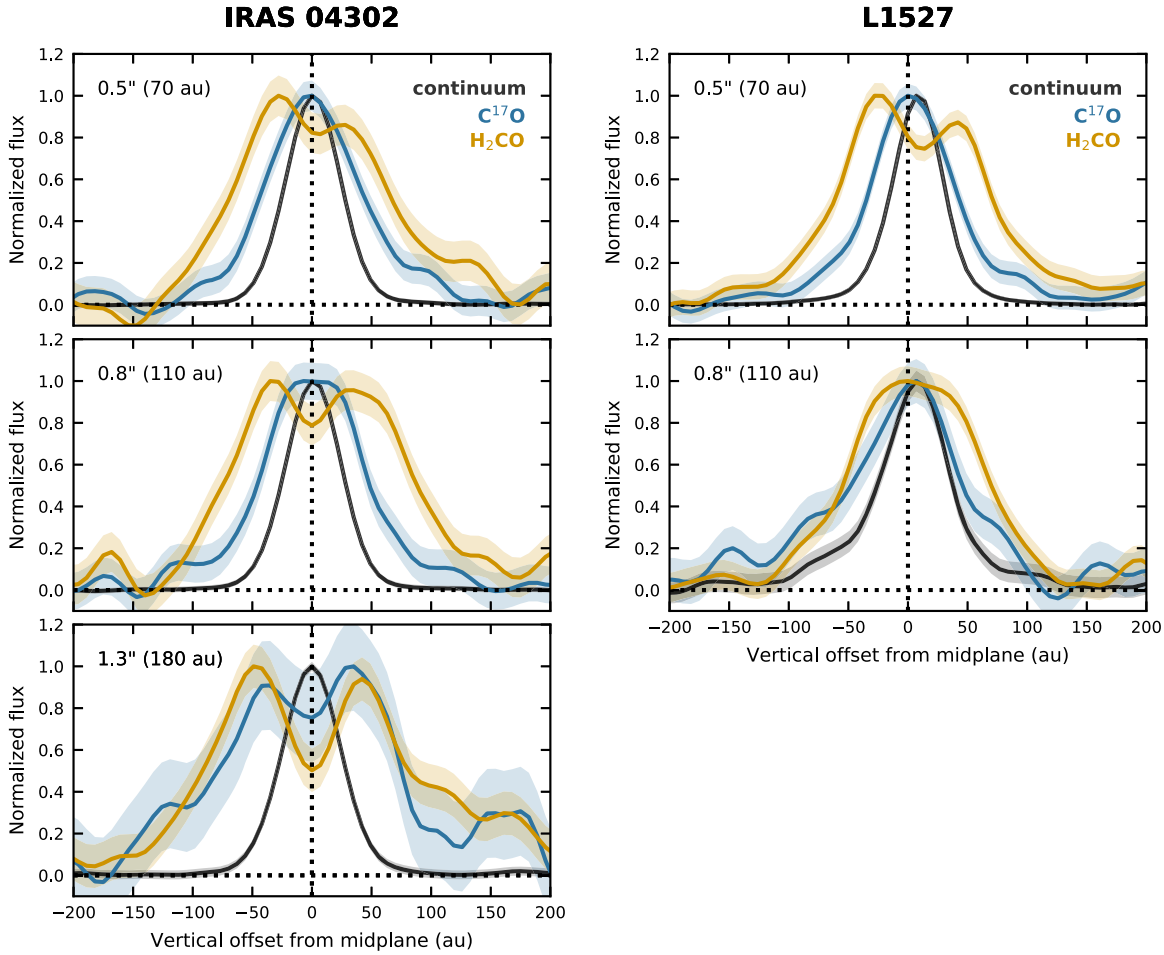

Figure 6. Vertical cuts through the edge-on disks IRAS 04302 (left panels) and L1527 (right panels) at $0\farcs5$ (top panels), $0\farcs8$ (middle panels), and $1\farcs3$ (bottom panel) north of the continuum peak. The 1.3 mm continuum is shown in black, and the integrated intensity for $C^{17}O$ $J = 2 - 1$ and H_2CO $3_{1,2} - 2_{1,1}$ are shown in blue and orange, respectively. The shaded area shows the 3σ uncertainty. The largest offset is not shown for L1527 because the continuum and $C^{17}O$ emission reach the noise limit. The H_2CO emission is single-peaked at $\sim$10 au.

in the envelope. Instead of a clear V shape, the emission in the inner region forms two bright lanes along the continuum position. A similar pattern is seen in the individual channels. This suggests that the H_2CO snowline is unresolved at the current resolution and closer in than in IRAS 04302 ($\lesssim$25 au).

A zeroth-order estimate of the midplane temperature profile for IRAS 04302 can be made from these two snowline estimates using a radial power law, $T \propto R^{-q}$. For disks, often a power-law exponent q of 0.5 is assumed, but q can range between 0.33 and 0.75 (see, e.g., Adams & Shu 1986; Kenyon et al. 1993; Chiang & Goldreich 1997). A power law with $q = 0.75$ matches the two temperature estimates reasonably well (see Figure 7). This temperature profile is quite similar to the profile constructed for L1527 based on ^{13}CO and $C^{18}O$ temperature measurements (van 't Hoff et al. 2018a). The L1527 temperature profile predicts an H_2CO snowline radius of $\lesssim$10 au, consistent with the results derived above. Thus, IRAS 04302 is warm like L1527, with freeze-out occurring only in the outermost part of this large disk.

4.2. Temperature Structure in Less Inclined Disks

For less inclined disks, observing freeze-out directly is much harder; the projected area between the top and bottom layer becomes smaller (that is, the V shape becomes more narrow), therefore requiring higher spatial resolution to observe it. In addition, because now both the near and the far sides of the disk become visible, emission from the far side's surface layers can appear to come from the near side's midplane (see Figure C2 and Pinte et al. 2018), which makes a V shape due to emission originating only in the surface layers that are harder to observe. For the L1527 disk model, the intermediate and warm models become quite similar for an inclination of 60° at this angular resolution, and only a cold disk shows a clear V-shaped pattern (Figure 8).

Figure 9 shows the $C^{17}O$ moment zero maps for the intermediate inclined disks TMC1A and L1489. The disk size, stellar mass, and stellar luminosity of TMC1A are comparable to L1527. At intermediate velocities, there is no sign of a V-shaped pattern, so these observations do not suggest substantial freeze-out of CO in TMC1A. In order to constrain the CO snowline a little better, models were run with snowline locations of 31, 42, and 56 au (that is, in between the cold and intermediate models). All three models show a V shape, suggesting that the CO snowline is at radii $\gtrsim$70 au in TMC1A. This is consistent with the results from Aso et al. (2015), who found a temperature of 38 K at 100 au from fitting a disk model to ALMA $C^{18}O$ observations, and Harsono et al. (submitted), who found a temperature of 20 K at 115 au. There is no sign of a V-shaped pattern in the H_2CO emission.

For L1489, the intermediate velocities show a more complex pattern, with CO peaking close to the source and at larger offsets

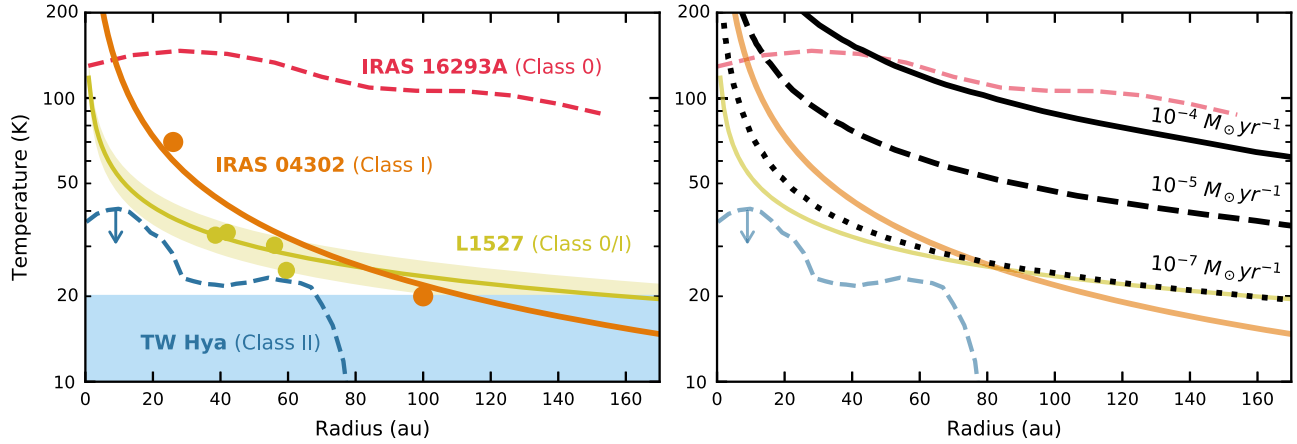

Figure 7. Left panel: radial midplane temperature profile for IRAS 04302 inferred from the CO and H_2CO snowline estimates (orange circles). The solid orange line is a power law of the shape $T \propto R^{-0.75}$. For comparison, the temperature measurements for L1527 from ^{13}CO and $C^{18}O$ emission (yellow circles) and a power-law temperature profile with $T \propto R^{-0.35}$ (yellow line; with 1σ uncertainty) are shown (van 't Hoff et al. 2018a), as well as the temperature profiles derived for the disklike structure in the Class 0 source IRAS 16293A (dashed red line; van 't Hoff et al. 2020) and the Class II disk TW Hya (dashed blue line; Schwarz et al. 2016). The TW Hya temperature profile traces a warmer layer above the midplane, and the midplane CO snowline is located at ~20 au (e.g., van 't Hoff et al. 2017; Zhang et al. 2017). The blue shaded area denotes the temperatures at which CO is frozen out. Right panel: temperature profiles from the left panel overlaid with temperature profiles from embedded disk models from Harsono et al. (2015). All three models have a stellar luminosity of 1 $L_\odot$, an envelope mass of 1 $M_\odot$, a disk mass of 0.05 $M_\odot$, and a disk radius of 200 au but different accretion rates of 10^{-4} (solid black line), 10^{-5} (dashed black line), and 10^{-7} (dotted black line) $M_\odot$ yr^{-1} and therefore different total luminosities.

($\gtrsim$2″). A similar structure was seen in $C^{18}O$ (Sai et al. 2020). This could be the result of nonthermal desorption of CO ice in the outer disk if the dust column is low enough for UV photons to penetrate (Cleeves 2016) or due to a radial temperature inversion resulting from radial drift and dust settling (Facchini et al. 2017). Such a double CO snowline has been observed for the protoplanetary disk IM Lup (Öberg et al. 2015; Cleeves 2016). The structure of the continuum emission, a bright central part and a fainter outer part, makes these plausible ideas. Another possibility is that the extended emission is due to a warm inner envelope component. The UV irradiated mass of L1489 derived from ^{13}CO 6–5 emission is similar to that of L1527 and higher than for TMC1A and TMC1 (Yıldız et al. 2015). This may provide a sufficient column along the outflow cavity wall for $C^{17}O$ emission to be observed. A high level of UV radiation is supported by O and H_2O line fluxes (Karska et al. 2018).

If the edge of the compact CO emission is due to freeze-out, the CO snowline is located at roughly 200 au. Models based on the continuum emission have temperatures of ~30 or ~20–30 K at 200 au (Brinch et al. 2007 and Sai et al. 2020, respectively), so CO could indeed be frozen out in this region. The H_2CO emission does not show a gap at 200 au, which could mean that the emission is coming from the surface layers. The $C^{17}O$ (and $C^{18}O$) abundance in these warmer surface layers may then be too low to be detected at the sensitivity of these observations.

5. Discussion

5.1. Temperature Structure of Young Disks

We have used observations of $C^{17}O$ and H_2CO toward five class I disks in Taurus to address whether embedded disks are warmer than more evolved Class II disks. While the $C^{17}O$ observations can indicate the presence or absence of $\lesssim$20 K gas, the addition of H_2CO observations allows one to further constrain the temperature profile. The picture that is emerging suggests that these young disks have midplanes with temperatures between ~20 and ~70 K: cold enough for H_2CO to freeze out but warm enough to retain CO in the gas phase (Figure 10). This suggests that, for example, the elemental C/O ratio in both the gas and ice could be different from that in protoplanetary disks. If planet formation starts during the embedded phase, the conditions for the first steps of grain growth are then different than generally assumed.

Young disks being warmer than protoplanetary disks can also have consequences for the derived disk masses from continuum fluxes. This has been taken into consideration in recent literature by adopting a dust temperature of 30 K for solar-luminosity protostars (Tobin et al. 2015, 2016b; Tychoniec et al. 2018; Tychoniec et al. 2020), although not uniformly (e.g., Andersen et al. 2019; Williams et al. 2019), while 20 K is generally assumed for protoplanetary disks (e.g., Ansdell et al. 2016). In their study of Orion protostars, Tobin et al. (2020) took this one step further by scaling the temperature by luminosity based on a grid of radiative transfer models resulting in an average temperature of 43 K for a 1 $L_\odot$ protostar. Since higher temperatures will result in lower masses for a certain continuum flux, detailed knowledge of the average disk temperature is crucial to determine the mass reservoir available for planet formation. While the current study shows that embedded disks are warmer than protoplanetary disks, and the radial temperature profiles for L1527 and IRAS 04302 hint that 30 K may be to low for the average disk temperature, source-specific modeling of the continuum and molecular line emission is required to address what would be an appropriate temperature to adopt for the mass derivation. However, an increase in temperature by a factor of 2 will lower the mass by only a factor of 2 (see Equation (2)), and Tobin et al. (2020) still found embedded disks to be more massive than protoplanetary disks by a factor >4. Differences in temperature can thus not account for the mass difference observed between embedded and protoplanetary disks.

5.1.1. The Textbook Example of IRAS 04302

The $C^{17}O$ and H_2CO emission toward IRAS 04302 presents a textbook example of what one would expect to observe for an edge-on disk, that is, a direct view of the vertical structure. The $C^{17}O$ emission is confined to the midplane, while H_2CO is tracing the surface layers. Assuming the absence of H_2CO

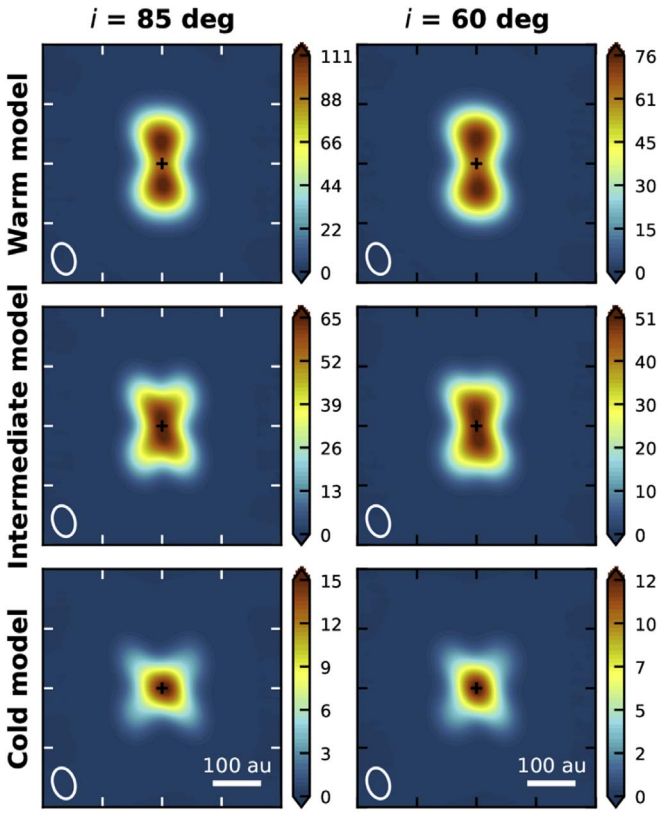

Figure 8. Integrated intensity (moment zero) maps of the intermediate-velocity $C^{17}O$ $J = 2 - 1$ emission in the warm (top row), intermediate (middle row), and cold (bottom row) disk models. The left column shows a near-edge-on disk ($i = 85°$), as in Figure 5, and the right column shows a less inclined disk ($i = 60°$). The velocity range Δv is 1.0–1.9 km s^{-1} for $i = 85°$ and 1.3–1.8 km s^{-1} for $i = 60°$. The color scale is in mJy beam^{-1} km s^{-1}. The source position is marked with a black plus sign, and the beam is shown in the lower left corner of the panels. A 100 au scale bar is present in the bottom panels.

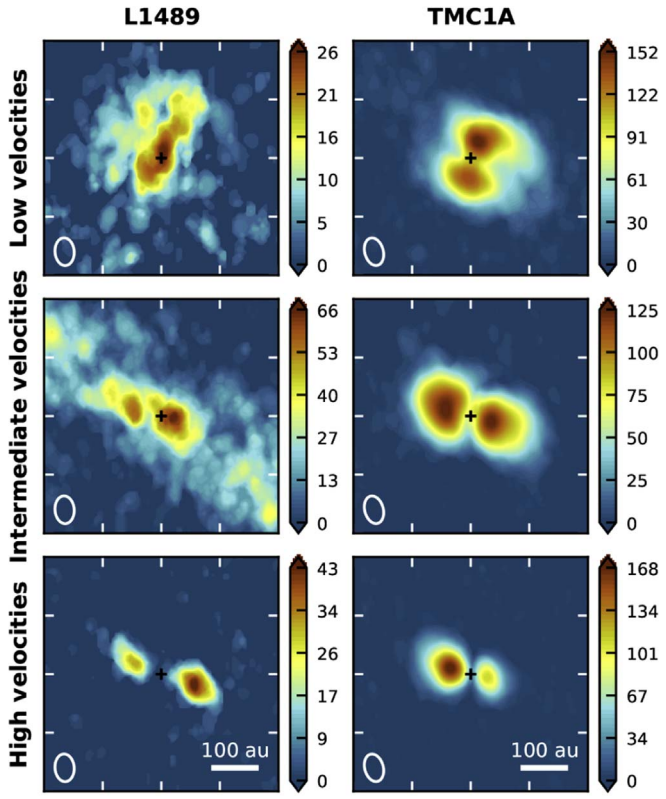

Figure 9. Integrated intensity (moment zero) maps of the low- (top row), intermediate- (middle row), and high- (bottom row) velocity $C^{17}O$ $J = 2 - 1$ emission toward L1489 (left column) and TMC1A (right column). Only pixels with $>3\sigma$ emission are included. For TMC1A (L1489), low velocities range from −1.27 to 1.26 (−0.47 to 0.43) km s^{-1}, the intermediate velocities include $|\Delta v| = 1.34–2.49$ (0.50–3.00) km s^{-1}, and the high velocities are $|\Delta v| = 2.57–4.94$ (3.05–4.65) km s^{-1} with respect to the source velocity. The color scale is in mJy beam^{-1} km s^{-1}. The source position is marked with a black plus sign, and the beam is shown in the lower left corner of the panels. A 100 au scale bar is present in the bottom panels.

emission in the midplane is due to freeze-out, we can make a first estimate not only of the radial temperature profile but also of the vertical temperature structure. At the current spatial resolution, the vertical structure is spatially resolved for radii $\gtrsim$70 au, that is, ∼three beams across the disk height. At these radii, the H_2CO emission peaks ∼30–50 au above the midplane (at radii of 70 and 180 au, respectively), suggesting that the temperature is between ∼20 and 70 K in the ∼30 au above the midplane.

The temperature structure can be further constrained by observing molecules with a freeze-out temperature between that of CO and H_2CO, that is, between ∼20 and 70 K. Based on the UMIST database for astrochemistry (McElroy et al. 2013), examples of such molecules are CN, CS, HCN, C_2H, SO, and H_2CS (in increasing order of freeze-out temperature). Another option would be to observe several H_2CO lines because their line ratios are a good indicator of the temperature (e.g., Mangum & Wootten 1993). These observations thus confirm that edge-on disks are well suited to study the disk vertical structure through molecular line observations.

5.1.2. Comparison with Protostellar Envelopes and Protoplanetary Disks

No sign of CO freeze-out is detected in the $C^{17}O$ observations of L1527, and while freeze-out is much more difficult to see in non-edge-on disks, TMC1A does not show hints of freeze-out at radii smaller than ∼70 au. A first estimate puts the CO snowline at ∼100 au in IRAS 04302, and the CO snowline may be located around ∼200 au in L1489. These young disks are thus warmer than T Tauri disks, where the snowline is typically at a few tens of au, as can be seen in Figure 11. We only include class II disks for which a CO snowline location has been reported based on molecular line observations, either $^{13}C^{18}O$ (for TW Hya; Zhang et al. 2017) or N_2H^+ (Qi et al. 2019). There is no clear trend between CO snowline location and bolometric luminosity for either Class, but the Class I disks have CO snow lines at larger radii compared to Class II disks with similar bolometric luminosities.

In protostellar envelopes, snowline radii larger than expected based on the luminosity have been interpreted as a sign of a recent accretion burst (Jørgensen et al. 2015; Frimann et al. 2017; Hsieh et al. 2019). During such a time period of increased accretion, the circumstellar material heats up, shifting the snow lines outward. Once the protostar returns to its quiescent stage, the temperature adopts almost instantaneously, while the chemistry takes longer to react. During this phase, the snow lines are at larger radii than expected from the luminosity. The results in Figure 11 could thus indicate that small accretion bursts have occurred in the Class I systems and that the CO snow lines have not yet shifted back to their quiescent location. When such a burst should have happened

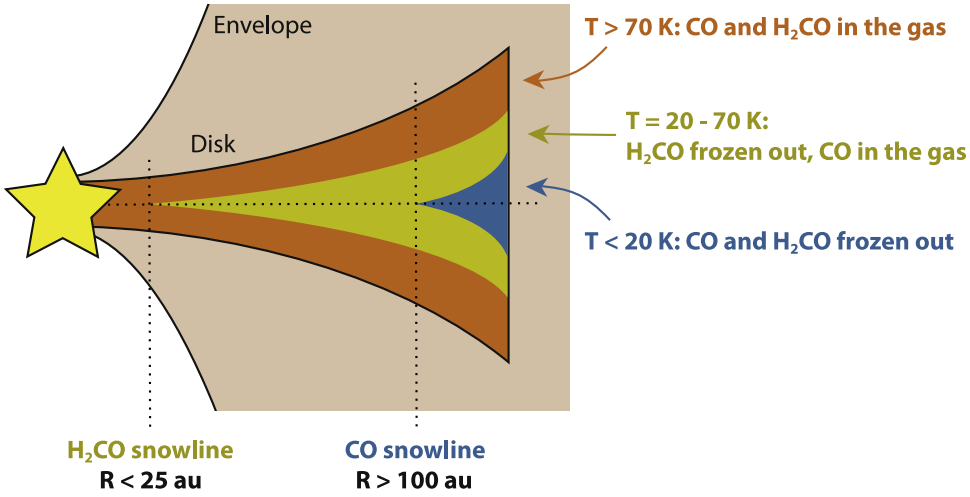

Figure 10. Schematic representation of the temperature structure derived for Class I disks based on $C^{17}O$ and H_2CO observations. A large part of the disk midplane, or even the entire midplane, is too warm for CO to freeze out, unlike protoplanetary disks that have the CO snowline at a few tens of au. The majority of the midplane has a temperature between ~20 and 70 K such that CO is in the gas phase while H_2CO is frozen out. The $C^{17}O$ emission therefore arises predominantly from the midplane region (yellow area), and the H_2CO emission arises from the surface layers (orange region).

depends on the freeze-out timescale, $\tau_{\rm fr}$,

$$\tau_{\rm fr} = 1 \times 10^4 \,{\rm yr} \sqrt{\frac{10\,{\rm K}}{T_{\rm fr}}} \frac{10^6\,{\rm cm}^{-3}}{n_{\rm H_2}}, \quad (4)$$

where $T_{\rm fr}$ is the freeze-out temperature and $n_{\rm H_2}$ is the gas density (Visser et al. 2012). For densities $\gtrsim 10^8\,{\rm cm}^{-3}$, the CO freeze-out timescale is $\lesssim$100 yr. This could suggest that Class I protostars frequently undergo small accretion bursts. Alternatively, these young disks may have lower densities than more evolved disks. As shown by the model results from N. M. Murillo et al. (2020, in preparation), decreasing the density while keeping the luminosity constant shifts the snow lines outward. If this is what is causing the results in Figure 11, this means that embedded disks not only have different temperature structures from protoplanetary disks but also have different density structures. However, the larger disk masses derived for embedded disks compared to protoplanetary disks for similar disk radii make this unlikely (Tobin et al. 2020).

Another comparison is made in Figure 7, where the radial temperature profiles inferred for L1527 and IRAS 04302 are shown together with those for the younger Class 0 disklike structure around IRAS 16293A (van 't Hoff et al. 2020) and the Class II disk TW Hya (Schwarz et al. 2016). The young disks are warmer than the more evolved Class II disk but much colder than the Class 0 system IRAS 16293A. When making this comparison, one should keep in mind that IRAS 16293A reflects an envelope where the temperature will be larger at larger scales because of the spherical rather than disk structure. In a disk, the temperature will drop more rapidly in the radial direction due to the higher extinction compared to an envelope. Nevertheless, such an evolutionary trend is expected because the accretion rate decreases as the envelope and disk dissipate. As a consequence, heating due to viscous accretion diminishes, and hence the temperature drops, as shown by two-dimensional physical and radiative transfer models for embedded protostars (D'Alessio et al. 1997; Harsono et al. 2015). In addition, the blanketing effect of the envelope decreases as the envelope dissipates (Whitney et al. 2003).

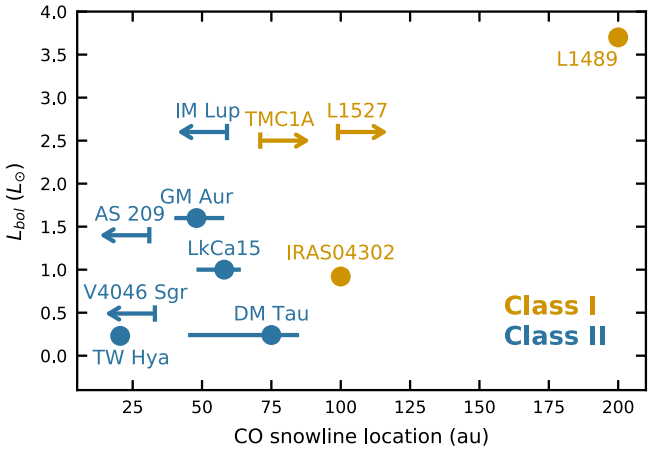

Figure 11. Overview of CO snowline locations in disks derived from molecular line observations as a function of bolometric luminosity. The locations for Class I disks (orange) are derived in this work using the $C^{17}O$ emission. Class II T Tauri disks are shown in blue. For TW Hya, the CO snowline location is determined from $^{13}C^{18}O$ emission by Zhang et al. (2017). For the other Class II disks, the CO snowline is derived from N_2H^+ emission by Qi et al. (2019). Arrows denote upper and lower limits.

As a first comparison between the observations and model predictions, models from Harsono et al. (2015) are overlaid on the observationally inferred temperature profiles in Figure 7 (right panel). In these models, the dust temperature is determined based on stellar irradiation and viscous accretion. Models are shown for a stellar luminosity of $1\,L_\odot$, an envelope mass of $1\,M_\odot$, a disk mass of $0.05\,M_\odot$, a disk radius of 200 au, and different accretion rates. The disk mass has a negligible effect on the temperature profiles (see Harsono et al. 2015 for details). The observations for IRAS 16293A match reasonably well with the temperature profile for a heavily accreting system ($10^{-4}\,M_\odot$ yr^{-1}), consistent with estimates of the accretion rate (e.g., $\sim 5 \times 10^{-5}\,M_\odot$ yr^{-1}; Schöier et al. 2002). However, because in these models, the total luminosity is based on the stellar and accretion luminosity (and a contribution from the disk), the match for IRAS 16239A with a strong accretion model may just reflect the system's bolometric luminosity of $20\,L_\odot$. In contrast, the temperature profiles for L1527 and IRAS 04302 are comparable to the colder $10^{-7}\,M_\odot$ yr^{-1} model, consistent with

the accretion rate of $\sim 3 \times 10^{-7}\,M_{\odot}\,\mathrm{yr}^{-1}$ for L1527 (see van 't Hoff et al. 2018a). Similar accretion rates on the order of $10^{-7}\,M_{\odot}\,\mathrm{yr}^{-1}$ have been reported for L1489, TMC1A, and TMC1 (e.g., Mottram et al. 2017; Yen et al. 2017) based on the bolometric luminosities (see, e.g., Stahler et al. 1980; Palla & Stahler 1993). We are not aware of a measurement toward IRAS 04302, but our very preliminary modeling results (M. L. R. van 't Hoff et al. 2020, in preparation) are consistent with an accretion rate on the order of $10^{-7}\,M_{\odot}\,\mathrm{yr}^{-1}$. Measured accretion rates for TW Hya range between $\sim 2 \times 10^{-10}$ and $2 \times 10^{-9}\,M_{\odot}\,\mathrm{yr}^{-1}$ (e.g., Herczeg & Hillenbrand 2008; Curran et al. 2011; Ingleby et al. 2013), and accretion rates of $\sim 10^{-10}$–$10^{-8}\,M_{\odot}\,\mathrm{yr}^{-1}$ are typically measured for protoplanetary disks around T Tauri stars (see Hartmann et al. 2016 for a review).

The results presented here thus provide observational evidence for cooling of the circumstellar material during evolution. More sources need to be observed to confirm this trend and answer more detailed questions, such as, when has a disk cooled down sufficiently for large-scale CO freeze-out? Does this already happen before the envelope dissipates? The object IRAS 04302 is a borderline Class I/Class II object embedded in the last remnants of its envelope, but it still has a temperature profile more similar to L1527 than TW Hya. Although a caveat here may be the old age of TW Hya (~10 Myr), this hints that disks may stay warm until the envelope has fully dissipated.

5.1.3. TMC1

For the first time, TMC1 is resolved to be a close (~85 au) binary. A possible configuration of the system could be that TMC1-E is present in the disk of TMC1-W, as observed, for example, for L1448 IRS3B (Tobin et al. 2016a). Then TMC1-E would increase the temperature on the east side of the disk. This may be an explanation for the asymmetry in the $C^{17}O$ emission with the emission dimmer east of TMC1-W (see Figures 3, A1 and A2). Given the upper-level energy of 16 K, emission from the $C^{17}O$ $J = 2 - 1$ transition will decrease with temperatures increasing above ~25 K. The weaker $C^{17}O$ emission may thus signal a higher temperature on the east side of the disk. However, TMC1-E does not seem to cause any disturbances in the disk, such as spiral arms, although the high inclination may make this hard to see. Another possibility could be that TMC1-E is actually in front of the disk.

5.2. Chemical Complexity in Young Disks

One of the major questions regarding the chemical composition of planetary material is whether it contains complex organic molecules (COMs). Due to the low temperatures in protoplanetary disks, observations of COMs are very challenging because these molecules thermally desorb at temperatures $\gtrsim$100–150 K, that is, in the inner few au. In contrast, COMs are readily detected on disk scales in protostellar envelopes (e.g., IRAS 16293, NGC1333 IRAS2A, NGC1333 IRAS4A, and B1-c; Taquet et al. 2015; Jørgensen et al. 2016; van Gelder et al. 2020) and in the young disk V883 Ori, where a luminosity outburst has heated the disk and liberated the COMs from the ice mantles (van 't Hoff et al. 2018b; Lee et al. 2019).

Although young disks seem warmer than protoplanetary disks, the CH_3OH and HDO nondetections with upper limits orders of magnitude below the column densities observed toward Class 0 protostellar envelopes suggest that they are not warm enough to have a hot core–like region with a large gas reservoir of COMs. This is consistent with recent findings by Artur de la Villarmois et al. (2019) for a sample of Class I protostars in Ophiuchus. More stringent upper limits are required for comparison with the Class II disks TW Hya and HD 163296. However, the detection of HDO and CH_3OH may have been hindered by optically thick dust in the inner region or the high inclinations of these sources. Modeling by N. M. Murillo et al. (2020, in preparation) shows that the water snowline is very hard to detect in near-edge-on disks. These nondetections thus do not rule out the presence of HDO and CH_3OH; in fact, if the region where HDO and CH_3OH are present is much smaller than the beam, they may have higher columns than the upper limits derived here. This is corroborated by the weak detection of CH_3OH in L1527 (Sakai et al. 2014a). These results thus merely show that Class I disks do not have an extended hot core–like region, making the detection of COMs just as challenging as in Class II disks.

A question related to the chemical composition is whether the disk material is directly inherited from the cloud, processed en route to the disk, or even fully reset upon entering the disk. Young disks like L1527, where no CO freeze-out is observed, suggest that no full inheritance takes place, at least not for the most volatile species like CO. Ice in the outer disk of IRAS 04302 could be inherited. However, the freeze-out timescale for densities $>10^6\,\mathrm{cm}^{-3}$ is $<10^4$ yr, so this CO could have sublimated upon entering the disk and frozen out as the disk cooled (see, e.g., Visser et al. 2009). Without CO ice, additional grain-surface formation of COMs will be limited in the young disks. So if COMs are present in more evolved disks, as, for example, shown for V883 Ori, they must have been inherited from a colder precollapse phase. Physicochemical models show that prestellar methanol can indeed be incorporated into the disk (Drozdovskaya et al. 2014).

5.3. Decrease in H_2CO in the Inner Disk

While the H_2CO emission is brighter than the $C^{17}O$ emission at intermediate velocities, no H_2CO emission is detected at the highest velocities in IRAS 04302, L1527, and TMC1A, suggesting a reduction in H_2CO flux in the inner $\lesssim$20–30 au in these disks. This is not just a sensitivity issue, as, for example, $C^{17}O$ and H_2CO have similar strengths and emitting areas in channels around $+1.9\,\mathrm{km\,s}^{-1}$ with respect to the source velocity in L1527, while $3.05\,\mathrm{km\,s}^{-1}$ is the highest velocity observed for $C^{17}O$ and $2.60\,\mathrm{km\,s}^{-1}$ the highest velocity for H_2CO. The decrease in H_2CO emission is also unlikely to be due to the continuum being optically thick because this would affect the $C^{17}O$ emission as well, unless there is significantly more $C^{17}O$ emission coming from layers above the dust millimeter $\tau = 1$ surface than H_2CO emission. Given the observed distributions, with H_2CO being vertically more extended than $C^{17}O$, this seems not to be the case. Moreover, the drop in H_2CO in TMC1A occurs much further out than where the dust becomes optically thick.

Formaldehyde rings have also been observed in the protoplanetary disks around TW Hya (Öberg et al. 2017), HD 163296 (Qi et al. 2013a; Carney et al. 2017), DM Tau (Henning & Semenov 2008; Loomis et al. 2015), and DG Tau (Podio et al. 2019). Interestingly, a ring is only observed for the $3_{03} - 2_{02}$ and $3_{12} - 2_{11}$ transitions and not for the $5_{15} - 4_{14}$ transition. Öberg et al. (2017) argued that the dust opacity cannot be the major contributor in TW Hya because the dust opacity should be higher at higher frequencies, thus for the $5_{15} - 4_{14}$

transition. Instead, they suggested a warm inner component that is visible in the $5_{15} - 4_{14}$ transition ($E_{up} = 63$ K) and not in the $3_{12} - 2_{11}$ transition ($E_{up} = 33$ K). For L1527, we observe the $3_{12} - 2_{11}$ transition, and radiative transfer modeling for the L1527 warm disk model shows that both the $C^{17}O$ ($E_{up} = 33$ K) and H_2CO emission go down by a factor of ~2 if the temperature is increased by 80%. An excitation effect thus seems unlikely, unless the $C^{17}O$ emission is optically thick. The latter is not expected, given that the $C^{18}O$ in L1527 is only marginally optically thick (van 't Hoff et al. 2018a). The absence of H_2CO emission in the inner disk thus points to a reduced H_2CO abundance. A lower total (gas + ice) H_2CO abundance (more than an order of magnitude) in the inner 30 au is seen in models by Visser et al. (2011), who studied the chemical evolution from prestellar core into disk, but these authors did not discuss the H_2CO chemistry.

The H_2CO abundance in the inner disk can be low if its formation is inefficient. It can form in both the gas and ice (e.g., Willacy & Woods 2009; Walsh et al. 2014; Loomis et al. 2015). On the grain surfaces, the dominant formation route is through hydrogenation of CO (Watanabe & Kouchi 2002; Cuppen et al. 2009; Fuchs et al. 2009). Since there seems to be no CO freeze-out in these young disks, or only at radii $\gtrsim$100 au, H_2CO is expected to form predominantly in the gas. Ring-shaped H_2CO emission due to increased ice formation outside the CO snowline, as used to explain the ring observed in HD 163296 (Qi et al. 2013a), is thus not applicable to the disks in this sample.

In the gas, the reaction between CH_3 and O is the most efficient way to form H_2CO (e.g., Loomis et al. 2015). Therefore, a decrease in gas-phase H_2CO formation would require a low abundance of either CH_3 or O. CH_3 is efficiently produced by photodissociation of CH_4 or through ion–molecule reactions. A low CH_3 abundance thus necessitates the majority of carbon to be present in CO, in combination with a low X-ray flux, as carbon can only be liberated from CO by X-ray-generated He^+. Atomic oxygen is formed through photodissociation of H_2O and CO_2 or dissociation of CO via X-ray-generated He^+. A low atomic oxygen abundance would thus require a low UV and X-ray flux.

Besides a low formation rate, a high destruction rate would also decrease the amount of H_2CO. However, the destruction products have a limited chemistry, and re-creation of H_2CO is the most likely outcome. Willacy & Woods (2009) showed that a third of the ions formed by H_2CO destruction through HCO^+ and DCO^+ form CO instead of reforming H_2CO, leading to a depletion between 7 and 20 au for their disk model. However, this only reduces H_2CO in the midplane, not in the surface layers. In addition, Henning & Semenov (2008) suggested the conversion of CO into CO_2-containing molecules and hydrocarbons that freeze out onto dust grains (see also Aikawa et al. 1999). However, the $C^{17}O$ observations do not suggest heavy CO depletion.

Another effect that could contribute is photodesorption of methanol ice that is inherited from earlier phases. Laboratory experiments have shown that methanol does not desorb intact upon vacuum ultraviolet (VUV) irradiation but rather leads to the release of smaller photofragments including H_2CO (Bertin et al. 2016; Cruz-Diaz et al. 2016). This could lead to an increase of H_2CO outside the region where CH_3OH ice thermally desorbs (~100–150 K). Finally, turbulence may play a role, as models by Furuya & Aikawa (2014) show the formation of H_2CO rings when mixing is included. However, these rings are due to a decrease of H_2CO inside the CO snowline and an increase outside this snowline, and these results may not be applicable to embedded disks without CO freeze-out. Observations of higher-excitation H_2CO lines and chemical modeling with source-specific structures may provide further insights.

It is worth noting that Pegues et al. (2020) found both centrally peaked and centrally depressed H_2CO emission profiles for a sample of 15 protoplanetary disks. A reduction of H_2CO emission toward three out of the five disks in our sample could mean that the H_2CO distribution is set during the embedded stage.

6. Conclusions

Temperature plays a key role in the physical and chemical evolution of circumstellar disks and therefore the outcome of planet formation. However, the temperature structure of young embedded disks, in which the first steps of planet formation take place, is poorly constrained. Our previous analysis of ^{13}CO and $C^{18}O$ emission in the young disk L1527 suggests that this disk is warm enough ($T \gtrsim$ 20–25 K) to prevent CO freeze-out (van 't Hoff et al. 2018a), in contrast to protoplanetary disks that show large cold outer regions where CO is frozen out. Here we present ALMA observations of $C^{17}O$ and H_2CO and nondetections of HDO and CH_3OH for five young disks in Taurus, including L1527. The observations of L1527 and, in particular, IRAS 04302, with $C^{17}O$ emission originating in the midplane and H_2CO emission tracing the surface layers, highlight the potential of edge-on disks to study the disk vertical structure.

Based on the following results, we conclude that young disks are likely warmer than more evolved protoplanetary disks but not warm enough to have a large gas reservoir of complex molecules, like the young disk around the outbursting star V883 Ori.

1. The presence of CO freeze-out can be directly observed with $C^{17}O$ observations in edge-on disks. The disk around L1527 shows no sign of CO freeze-out, but IRAS 04302 has a large enough disk for the temperature to drop below the CO freeze-out temperature in the outermost part (radii $\gtrsim$100 au).
2. The H_2CO emission originates primarily in the surface layers of IRAS 04302 and L1527. The snowline ($T \sim 70$ K) is estimated around (or inward of) ~25 au in IRAS 04302 and at $\lesssim$25 au in L1527.
3. The presence of CO freeze-out is much more difficult to observe in non-edge-on disks, but the $C^{17}O$ emission in TMC1A suggest a snowline at radii $\gtrsim$70 au. Two spatial components are seen in the $C^{17}O$ emission toward L1489. If the outer edge of the inner component is due to CO freeze-out, the snowline will be around ~200 au.
4. The CO snowline locations derived for the Class I disks are farther out than those found for Class II disks with similar bolometric luminosities.
5. The HDO and CH_3OH nondetections with upper limits more than 2 orders of magnitude lower than those observed for hot cores in protostellar envelopes or the disk around the outbursting star V883 Ori suggest that these Class I disks do not have a large gas reservoir of COMs.
6. The inferred temperature profiles are consistent with trends found in radiative transfer models of disk–envelope systems with accretion rates decreasing from 10^{-4} to 10^{-7} $M_\odot$ yr^{-1}.

As evidence is piling up for planet formation to start already during the embedded phase, adopting initial conditions based on the physical conditions in more evolved Class II disks seems inappropriate. Instead, planet formation may start in warmer

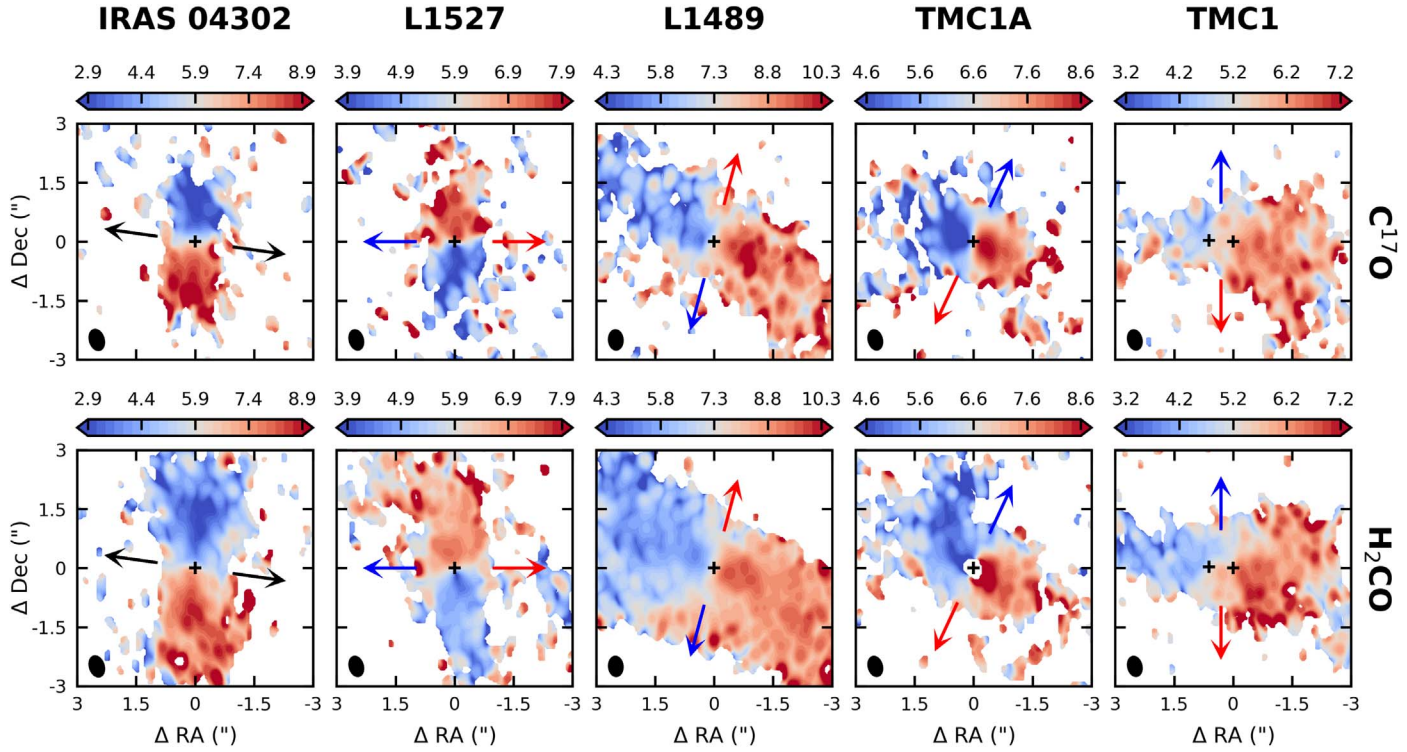

Figure A1. Moment one maps for the $C^{17}O$ $J = 2 - 1$ (top row) and H_2CO $3_{1,2} - 2_{1,1}$ (bottom row) transitions. The central velocity of the color scale is the systemic velocity (km s^{-1}). The positions of the continuum peaks are marked with black plus signs, and the outflow directions are indicated by arrows. The beam is shown in the lower left corner of each panel.

conditions than generally assumed. Furthermore, without a large CO-ice reservoir, COM formation efficiency is limited in embedded disks. Observations of COMs in more evolved disks therefore suggest that these molecules are inherited from earlier phases.

We would like to thank the referee for a prompt and positive report that helped improve the paper, Patrick Sheehan for his assistance with the visibility plotting, and Gleb Fedoseev for useful discussions about the H_2CO freeze-out temperature. M.L. R.H. would like to thank Yuri Aikawa for comments on an earlier version of this manuscript for her PhD thesis. This paper makes use of the following ALMA data: ADS/JAO. ALMA#2017.1.01413.S. ALMA is a partnership of ESO (representing its member states), NSF (USA), and NINS (Japan), together with NRC (Canada), MOST and ASIAA (Taiwan), and KASI (Republic of Korea), in cooperation with the Republic of Chile. The Joint ALMA Observatory is operated by ESO, AUI/NRAO, and NAOJ. Astrochemistry in Leiden is supported by the Netherlands Research School for Astronomy (NOVA). M.L. R.H. acknowledges support from a Huygens fellowship from Leiden University. J.J.T. acknowledges support from grant AST-1814762 from the National Science Foundation and past support from the Homer L. Dodge Endowed Chair at the University of Oklahoma. The National Radio Astronomy Observatory is a facility of the National Science Foundation operated under cooperative agreement by Associated Universities, Inc. J.K.J. acknowledges support by the European Research Council (ERC) under the European Union's Horizon 2020 research and innovation program through ERC Consolidator Grant "S4F" (grant agreement No. 646908). A.M. acknowledges funding from the European Union's Horizon 2020 research and innovation program under Marie Sklodowska-Curie grant agreement No. 823823 (RISE DUSTBUSTERS) and from the Deutsche Forschungsgemeinschaft (DFG; German Research Foundation), Ref. no. FOR 2634/1 ER685/11-1. C.W. acknowledges financial support from the University of Leeds and the Science and Technology Facilities Council (grant Nos. ST/R000549/1 and ST/T000287/1).

Table A1
Overview of the Molecular Line Observations

Molecule	Transition	Frequency (GHz)	A_{ul}[a] (s^{-1})	E_{up}[b] (K)
$C^{17}O$	$2 - 1$	224.714385	6.42×10^{-7}	16
H_2CO	$3_{1,2} - 2_{1,1}$	225.697775	2.77×10^{-4}	33
HDO	$3_{1,2} - 2_{2,1}$	225.896720	1.32×10^{-5}	168
CH_3OH	$5 - 4$[c]	241.820762[d]	$2–6 \times 10^{-5}$	34–131

Notes. Data for $C^{17}O$ and HDO are taken from the Jet Propulsion Laboratory Molecular Spectroscopy database (Pickett et al. 1998), and data for H_2CO and CH_3OH are from the Cologne Database for Molecular Spectroscopy (Müller et al. 2005).
[a] Einstein A coefficient.
[b] Upper-level energy.
[c] The spectral window covers multiple transitions in the $5_K - 4_K$ branch for both A- and E-methanol (16 transitions in total).
[d] Central frequency of the spectral window.

Appendix A
Observations

Table A1 presents an overview of the observed molecular lines. Moment one maps for $C^{17}O$ and H_2CO toward all disks in the sample are shown in Figure A1, and spectra integrated over pixels with $>3\sigma$ emission in a 6″ circular aperture are presented in Figure A2.

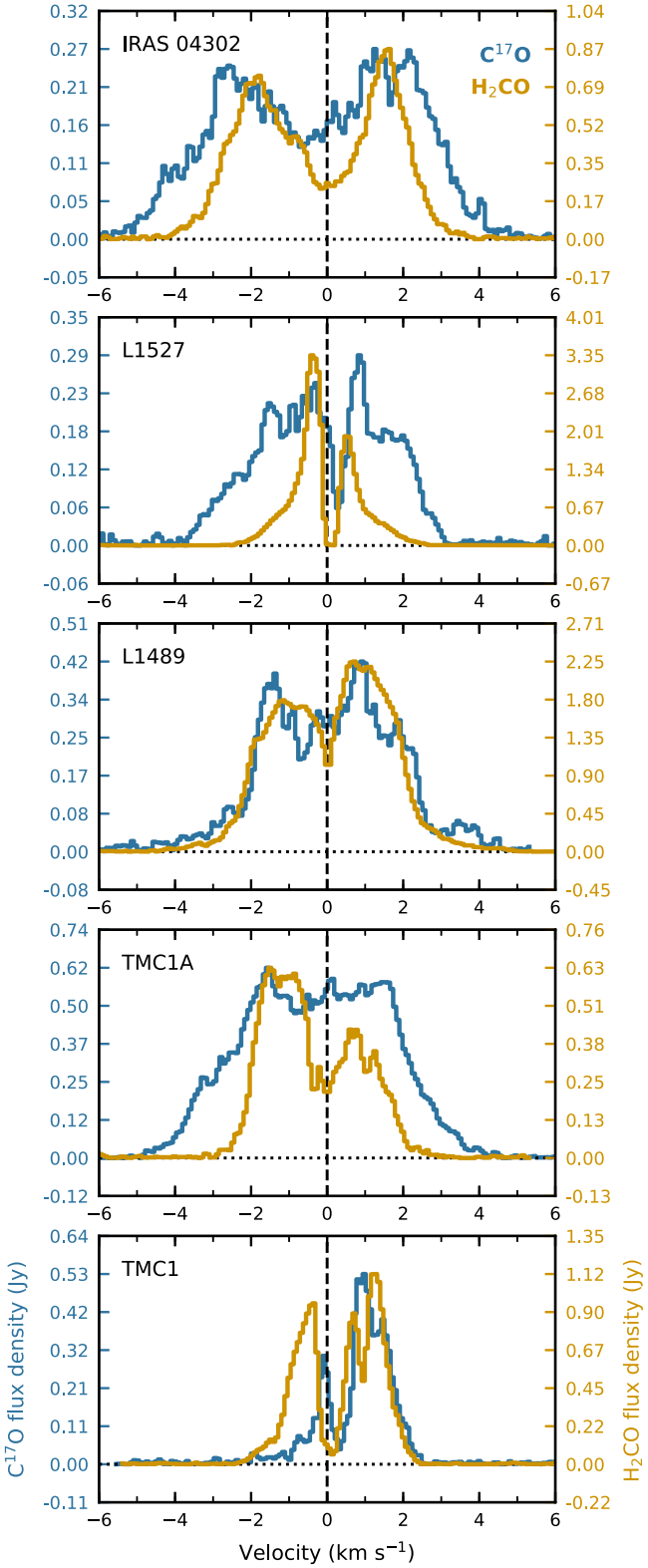

Figure A2. Spectra for $C^{17}O$ (blue) and H_2CO (orange) extracted in a 6″ circular aperture centered at the continuum peak. Only pixels with $>3\sigma$ emission are included. The vertical scale is different for each molecular line in each panel. The vertical dashed lines mark the systemic velocities, which have been shifted to 0 km s^{-1}.

Appendix B
Envelope Contribution

A first assessment of the envelope contribution to the line emission can be made by comparing generic models of either a Keplerian disk only or a disk embedded in an envelope to the observed visibility amplitudes. To do so, we calculated the visibility amplitude profiles for a Keplerian disk in 0.5 km s^{-1} channels using the modeling tools outlined in Sheehan et al. (2019). Values for the stellar mass, disk radius, inclination, and position angle were adopted from the

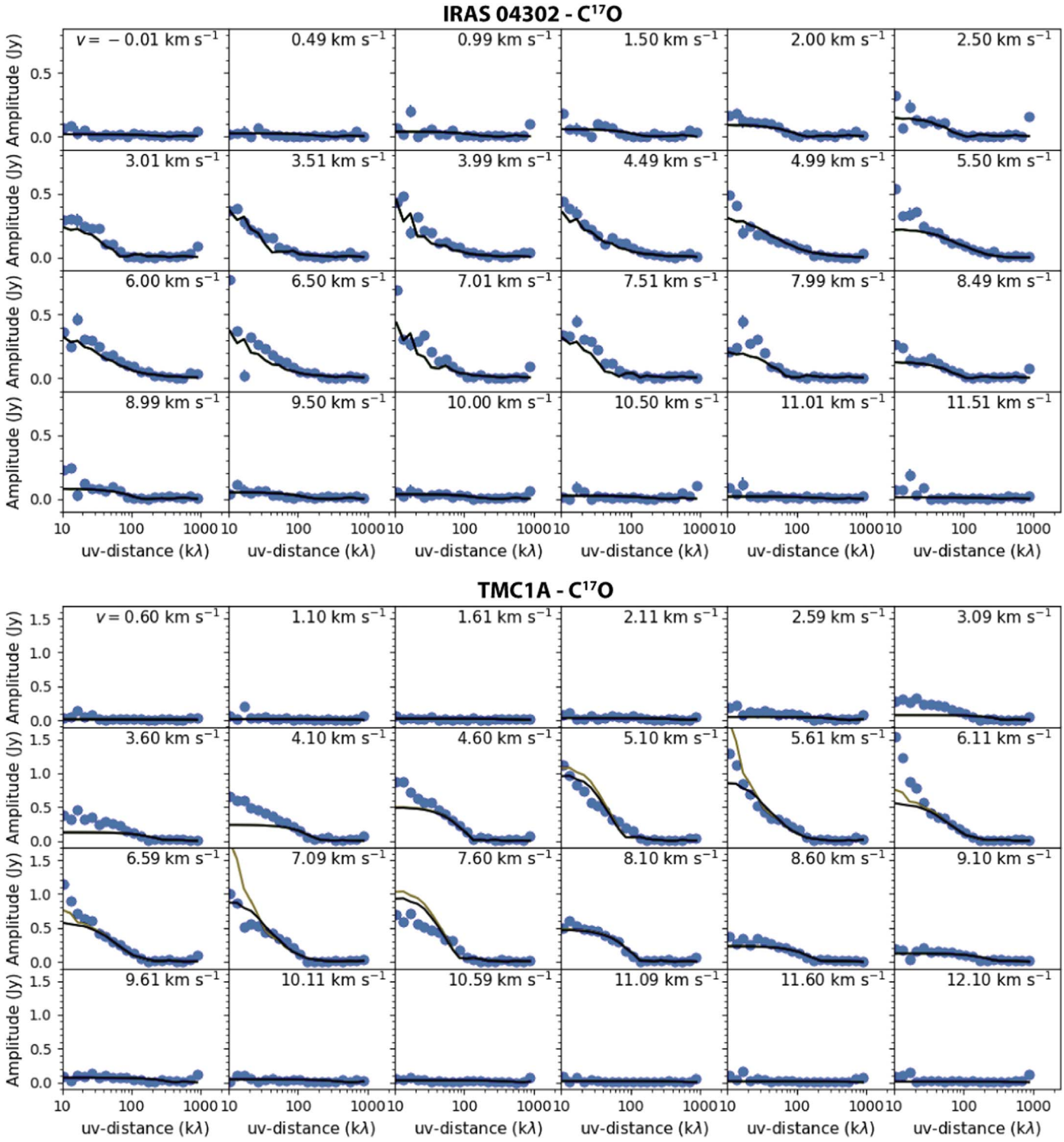

Figure B1. Visibility amplitude profiles for $C^{17}O$ toward IRAS 04302 (top panels) and TMC1A (bottom panels). The black line displays a Keplerian disk, and the orange line represents a Keplerian disk plus rotating infalling envelope (Ulrich 1976). The systemic velocities are 5.9 and 6.6 km s^{-1} for IRAS 04302 and TMC1A, respectively.

literature, and the $C^{17}O$ and H_2CO abundances were taken as constant throughout the disk. The disk mass was adjusted to approximately match the visibility amplitude profiles in each channel. If there was a component at small uv-distances that could not be reproduced with the disk, we added a rotating infalling envelope with a 3000 au radius using the prescription by Ulrich (1976). The results for $C^{17}O$ toward IRAS 04302 and TMC1A are shown as an example in Figure B1. We stress that we do not expect a perfect fit with this simple approach, but it shows that the $C^{17}O$ emission toward IRAS 04302 can be reproduced without an envelope, while some envelope contribution is required at low velocities ($\sim|1|$ km s^{-1} from the systemic velocity) toward TMC1A.

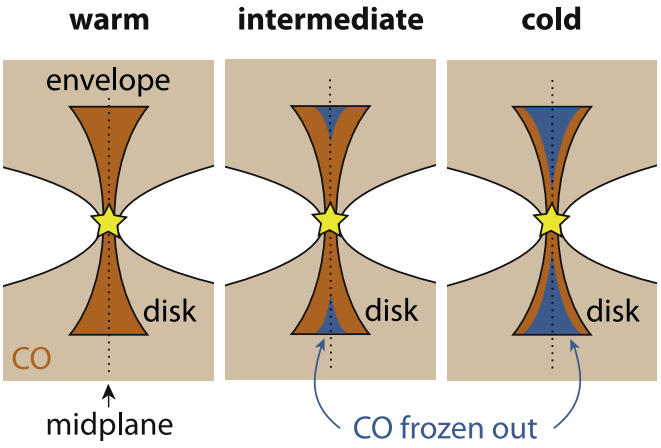

Figure C1. Three different models for the CO distribution in embedded disks. Left panel: warm disk with no CO freeze-out. Middle panel: slightly colder disk where CO is frozen out in the outer disk midplane. Right panel: cold disk where gaseous CO is only present in the inner disk and disk surface layers. Gaseous CO is present in the inner envelope in all models. Figure reproduced from van 't Hoff et al. (2018a).

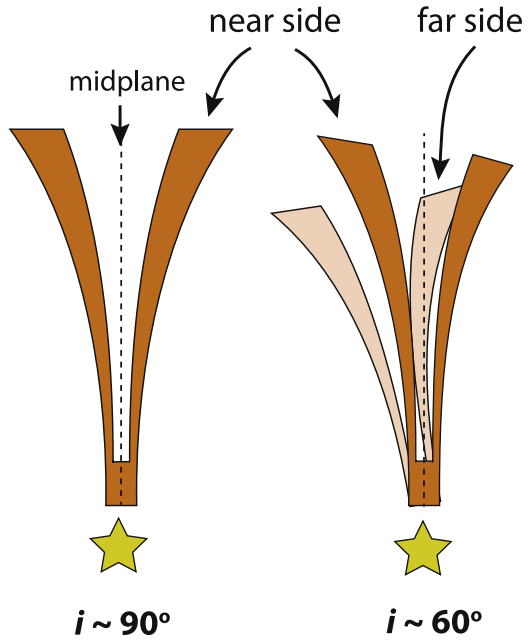

Figure C2. Schematic representation of a disk with emission originating only in the surface layers viewed edge-on (~90°; left panel) and at an inclination of ~60° (right panel). In the edge-on orientation, only the near side of the disk is visible, and at sufficient angular resolution, a V-shaped emission pattern is observed. In contrast, when the disk is ~60° inclined, the far side of the disk becomes visible, and emission from the far side appears to be coming from the midplane. This is especially problematic at low angular resolution, when the continuum disk is too small to map out the midplane or the line is too weak to be detected in individual channels at high enough spectral resolution.

Appendix C
Schematics of the Disk Models

Figure C1 shows a schematic overview of the warm, intermediate, and cold disk models as presented by van 't Hoff et al. (2018a). In the warm model, CO is present in the gas phase in the entire disk, whereas in the cold model, CO is frozen out in most of the disk, with gas-phase CO only present in the inner disk and disk surface layers. In the intermediate model, CO freeze-out occurs in the outer midplane. A constant gas-phase CO abundance of 10^{-4} with respect to H_2 is adopted in the regions where $T > 20$ K. If the envelope is included in the radiative transfer, gas-phase CO is present in the $T > 20$ K region at an abundance of 10^{-4} as well. For the physical structure (dust density and temperature), we adopt the model for L1527 from Tobin et al. (2013), who modeled the disk continuum emission by fitting both the visibilities and images of 870 μm and 3.4 mm observations, the multiwavelength spectral energy distribution, and L' scattered-light images with 3D radiative transfer modeling.

Figure C2 illustrates why observing freeze-out directly can be challenging in disks that are not viewed edge-on.

ORCID iDs

Merel L. R. van 't Hoff https://orcid.org/0000-0002-2555-9869
Daniel Harsono https://orcid.org/0000-0001-6307-4195
John J. Tobin https://orcid.org/0000-0002-6195-0152
Arthur D. Bosman https://orcid.org/0000-0003-4001-3589
Ewine F. van Dishoeck https://orcid.org/0000-0001-7591-1907
Jes K. Jørgensen https://orcid.org/0000-0001-9133-8047
Anna Miotello https://orcid.org/0000-0002-7997-2528
Catherine Walsh https://orcid.org/0000-0001-6078-786X

References

Adams, F. C., & Shu, F. H. 1986, ApJ, 308, 836
Aikawa, Y., Umebayashi, T., Nakano, T., & Miyama, S. M. 1999, ApJ, 519, 705
Aikawa, Y., van Zadelhoff, G. J., van Dishoeck, E. F., & Herbst, E. 2002, A&A, 386, 622
Ali-Dib, M. 2017, MNRAS, 467, 2845
ALMA Partnership, Brogan, C. L., Pérez, L. M., et al. 2015, ApJL, 808, L3
Andersen, B. C., Stephens, I. W., Dunham, M. M., et al. 2019, ApJ, 873, 54
Andrews, S. M., Huang, J., Pérez, L. M., et al. 2018, ApJL, 869, L41
Andrews, S. M., Wilner, D. J., Hughes, A. M., Qi, C., & Dullemond, C. P. 2010, ApJ, 723, 1241
Ansdell, M., Williams, J. P., Manara, C. F., et al. 2017, AJ, 153, 240
Ansdell, M., Williams, J. P., van der Marel, N., et al. 2016, ApJ, 828, 46
Artur de la Villarmois, E., Jørgensen, J. K., Kristensen, L. E., et al. 2019, A&A, 626, A71
Aso, Y., Ohashi, N., Aikawa, Y., et al. 2017, ApJ, 849, 56
Aso, Y., Ohashi, N., Saigo, K., et al. 2015, ApJ, 812, 27
Barenfeld, S. A., Carpenter, J. M., Ricci, L., & Isella, A. 2016, ApJ, 827, 142
Bergin, E. A., Cleeves, L. I., Crockett, N., & Blake, G. A. 2014, FaDi, 168, 61
Bergner, J. B., Guzmán, V. G., Öberg, K. I., Loomis, R. A., & Pegues, J. 2018, ApJ, 857, 69
Bergner, J. B., Oberg, K. I., Bergin, E. A., et al. 2020, ApJ, 898, 97
Bertin, M., Romanzin, C., Doronin, M., et al. 2016, ApJL, 817, L12
Boley, A. C. 2009, ApJL, 695, L53
Boogert, A. C. A., Gerakines, P. A., & Whittet, D. C. B. 2015, ARA&A, 53, 541
Bosman, A. D., Walsh, C., & van Dishoeck, E. F. 2018, A&A, 618, A182
Boss, A. P. 1997, Sci, 276, 1836
Brinch, C., Crapsi, A., Jørgensen, J. K., Hogerheijde, M. R., & Hill, T. 2007, A&A, 475, 915
Brinch, C., & Hogerheijde, M. R. 2010, A&A, 523, A25
Carney, M. T., Hogerheijde, M. R., Guzmán, V. V., et al. 2019, A&A, 623, A124
Carney, M. T., Hogerheijde, M. R., Loomis, R. A., et al. 2017, A&A, 605, A21
Chiang, E. I., & Goldreich, P. 1997, ApJ, 490, 368
Chuang, K.-J., Fedoseev, G., Ioppolo, S., van Dishoeck, E. F., & Linnartz, H. 2016, MNRAS, 455, 1702
Cieza, L. A., Ruíz-Rodríguez, D., Hales, A., et al. 2019, MNRAS, 482, 698
Cleeves, L. I. 2016, ApJL, 816, L21
Cleeves, L. I., Bergin, E. A., Qi, C., Adams, F. C., & Öberg, K. I. 2015, ApJ, 799, 204
Cox, E. G., Harris, R. J., Looney, L. W., et al. 2017, ApJ, 851, 83
Cridland, A. J., Eistrup, C., & van Dishoeck, E. F. 2019, A&A, 627, A127

Cruz-Diaz, G. A., Martín-Doménech, R., Muñoz Caro, G. M., & Chen, Y. J. 2016, A&A, 592, A68
Cuppen, H. M., van Dishoeck, E. F., Herbst, E., & Tielens, A. G. G. M. 2009, A&A, 508, 275
Curran, R. L., Argiroffi, C., Sacco, G. G., et al. 2011, A&A, 526, A104
D'Alessio, P., Calvet, N., & Hartmann, L. 1997, ApJ, 474, 397
Drążkowska, J., & Alibert, Y. 2017, A&A, 608, A92
Drozdovskaya, M. N., Walsh, C., Visser, R., Harsono, D., & van Dishoeck, E. F. 2014, MNRAS, 445, 913
Dutrey, A., Guilloteau, S., & Guelin, M. 1997, A&A, 317, L55
Dutrey, A., Guilloteau, S., Piétu, V., et al. 2017, A&A, 607, 130
Eistrup, C., Walsh, C., & van Dishoeck, E. F. 2016, A&A, 595, A83
Facchini, S., Birnstiel, T., Bruderer, S., & van Dishoeck, E. F. 2017, A&A, 605, A16
Favre, C., Cleeves, L. I., Bergin, E. A., Qi, C., & Blake, G. A. 2013, ApJL, 776, L38
Favre, C., Fedele, D., Semenov, D., et al. 2018, ApJL, 862, L2
Fedoseev, G., Cuppen, H. M., Ioppolo, S., Lamberts, T., & Linnartz, H. 2015, MNRAS, 448, 1288
Frimann, S., Jørgensen, J. K., Dunham, M. M., et al. 2017, A&A, 602, A120
Fuchs, G. W., Cuppen, H. M., Ioppolo, S., et al. 2009, A&A, 505, 629
Furuya, K., & Aikawa, Y. 2014, ApJ, 790, 97
Garrod, R. T., & Herbst, E. 2006, A&A, 457, 927
Green, J. D., Evans, N. J. I., Jørgensen, J. K., et al. 2013, ApJ, 770, 123
Harsono, D., Bjerkeli, P., van der Wiel, M. H. D., et al. 2018, NatAs, 2, 646
Harsono, D., Bruderer, S., & van Dishoeck, E. F. 2015, A&A, 582, A41
Harsono, D., Jørgensen, J. K., van Dishoeck, E. F., et al. 2014, A&A, 562, A77
Hartmann, L., Herczeg, G., & Calvet, N. 2016, ARA&A, 54, 135
Henning, T., & Semenov, D. 2008, in IAU Symp. 251, Organic Matter in Space, ed. S. Kwok & S. Sanford (Cambridge: Cambridge Univ. Press), 89
Herczeg, G. J., & Hillenbrand, L. A. 2008, ApJ, 681, 594
Hildebrand, R. H. 1983, QJRAS, 24, 267
Hsieh, T.-H., Murillo, N. M., Belloche, A., et al. 2019, ApJ, 884, 149
Huang, J., Öberg, K. I., Qi, C., et al. 2017, ApJ, 835, 231
Ingleby, L., Calvet, N., Herczeg, G., et al. 2013, ApJ, 767, 112
Jørgensen, J. K., Bourke, T. L., Myers, P. C., et al. 2007, ApJ, 659, 479
Jørgensen, J. K., van der Wiel, M. H. D., Coutens, A., et al. 2016, A&A, 595, A117
Jørgensen, J. K., van Dishoeck, E. F., Visser, R., et al. 2009, A&A, 507, 861
Jørgensen, J. K., Visser, R., Williams, J. P., & Bergin, E. A. 2015, A&A, 579, A23
Kama, M., Bruderer, S., van Dishoeck, E. F., et al. 2016, A&A, 592, A83
Karska, A., Kaufman, M. J., Kristensen, L. E., et al. 2018, ApJS, 235, 30
Kenyon, S. J., Calvet, N., & Hartmann, L. 1993, ApJ, 414, 676
Kratter, K., & Lodato, G. 2016, ARA&A, 54, 271
Krijt, S., Schwarz, K. R., Bergin, E. A., & Ciesla, F. J. 2018, ApJ, 864, 78
Kristensen, L. E., van Dishoeck, E. F., Bergin, E. A., et al. 2012, A&A, 542, A8
Kwon, W., Looney, L. W., Mundy, L. G., Chiang, H.-F., & Kemball, A. J. 2009, ApJ, 696, 841
Lee, J.-E., Lee, S., Baek, G., et al. 2019, NatAs, 3, 314
Long, F., Herczeg, G. J., Pascucci, I., et al. 2017, ApJ, 844, 99
Loomis, R. A., Cleeves, L. I., Öberg, K. I., et al. 2018, ApJ, 859, 131
Loomis, R. A., Cleeves, L. I., Öberg, K. I., Guzman, V. V., & Andrews, S. M. 2015, ApJL, 809, L25
Madhusudhan, N., Amin, M. A., & Kennedy, G. M. 2014, ApJL, 794, L12
Manara, C. F., Morbidelli, A., & Guillot, T. 2018, A&A, 618, L3
Manara, C. F., Rosotti, G., Testi, L., et al. 2016, A&A, 591, L3
Mangum, J. G., & Wootten, A. 1993, ApJS, 89, 123
Mathews, G. S., Klaassen, P. D., Juhász, A., et al. 2013, A&A, 557, A132
McClure, M. K., Bergin, E. A., Cleeves, L. I., et al. 2016, ApJ, 831, 167
McElroy, D., Walsh, C., Markwick, A. J., et al. 2013, A&A, 550, A36
McMullin, J. P., Waters, B., Schiebel, D., Young, W., & Golap, K. 2007, in ASP Conf. Ser. 376, Astronomical Data Analysis Software and Systems XVI, ed. R. A. Shaw, F. Hill, & D. J. Bell (San Francisco, CA: ASP), 127
Miotello, A., Testi, L., Lodato, G., et al. 2014, A&A, 567, A32
Miotello, A., van Dishoeck, E. F., Williams, J. P., et al. 2017, A&A, 599, A113
Motte, F., & André, P. 2001, A&A, 365, 440
Mottram, J. C., van Dishoeck, E. F., Kristensen, L. E., et al. 2017, A&A, 600, A99
Müller, H. S. P., Schlöder, F., Stutzki, J., & Winnewisser, G. 2005, JMoSt, 742, 215
Murillo, N. M., Bruderer, S., van Dishoeck, E. F., et al. 2015, A&A, 579, A114
Murillo, N. M., Lai, S.-P., Bruderer, S., Harsono, D., & van Dishoeck, E. F. 2013, A&A, 560, A103
Noble, J. A., Theule, P., Mispelaer, F., et al. 2012, A&A, 543, A5
Öberg, K. I., Furuya, K., Loomis, R., et al. 2015, ApJ, 810, 112
Öberg, K. I., Guzmán, V. V., Merchantz, C. J., et al. 2017, ApJ, 839, 43
Öberg, K. I., Murray-Clay, R., & Bergin, E. A. 2011, ApJL, 743, L16
Öberg, K. I., Qi, C., Fogel, J. K. J., et al. 2010, ApJ, 720, 480
Ohashi, N., Saigo, K., Aso, Y., et al. 2014, ApJ, 796, 131
Oya, Y., Sakai, N., Lefloch, B., et al. 2015, ApJ, 812, 59
Oya, Y., Sakai, N., López-Sepulcre, A., et al. 2016, ApJ, 824, 88
Palla, F., & Stahler, S. W. 1993, ApJ, 418, 414
Pascucci, I., Testi, L., Herczeg, G. J., et al. 2016, ApJ, 831, 125
Pegues, J., Öberg, K. I., Bergner, J. B., et al. 2020, ApJ, 890, 142
Persson, M. V., Jørgensen, J. K., & van Dishoeck, E. F. 2013, A&A, 549, L3
Persson, M. V., Jørgensen, J. K., van Dishoeck, E. F., & Harsono, D. 2014, A&A, 563, A74
Pickett, H. M., Poynter, R. L., Cohen, E. A., et al. 1998, JQSRT, 60, 883
Pinte, C., Ménard, F., Duchêne, G., et al. 2018, A&A, 609, A47
Podio, L., Bacciotti, F., Fedele, D., et al. 2019, A&A, 623, L6
Qi, C., Öberg, K. I., Andrews, S. M., et al. 2015, ApJ, 813, 128
Qi, C., Öberg, K. I., Espaillat, C. C., et al. 2019, ApJ, 882, 160
Qi, C., Öberg, K. I., & Wilner, D. J. 2013a, ApJ, 765, 34
Qi, C., Öberg, K. I., Wilner, D. J., et al. 2013b, Sci, 341, 630
Ruíz-Rodríguez, D., Cieza, L. A., Williams, J. P., et al. 2018, MNRAS, 478, 3674
Sai, J., Ohashi, N., Saigo, K., et al. 2020, ApJ, 893, 51
Sakai, N., Oya, Y., Sakai, T., et al. 2014a, ApJL, 791, L38
Sakai, N., Sakai, T., Hirota, T., et al. 2014b, Natur, 507, 78
Schöier, F. L., Jørgensen, J. K., van Dishoeck, E. F., & Blake, G. A. 2002, A&A, 390, 1001
Schöier, F. L., van der Tak, F. F. S., van Dishoeck, E. F., & Black, J. H. 2005, A&A, 432, 369
Schoonenberg, D., & Ormel, C. W. 2017, A&A, 602, A21
Schwarz, K. R., Bergin, E. A., Cleeves, L. I., et al. 2016, ApJ, 823, 91
Schwarz, K. R., Bergin, E. A., Cleeves, L. I., et al. 2018, ApJ, 856, 85
Schwarz, K. R., Bergin, E. A., Cleeves, L. I., et al. 2019, ApJ, 877, 131
Sheehan, P. D., & Eisner, J. A. 2017, ApJ, 851, 45
Sheehan, P. D., Wu, Y.-L., Eisner, J. A., & Tobin, J. J. 2019, ApJ, 874, 136
Stahler, S. W., Shu, F. H., & Taam, R. E. 1980, ApJ, 241, 637
Stevenson, D. J., & Lunine, J. I. 1988, Icar, 75, 146
Taquet, V., López-Sepulcre, A., Ceccarelli, C., et al. 2013, ApJL, 768, L29
Taquet, V., López-Sepulcre, A., Ceccarelli, C., et al. 2015, ApJ, 804, 81
Thi, W.-F., van Zadelhoff, G.-J., & van Dishoeck, E. F. 2004, A&A, 425, 955
Tielens, A. G. G. M., & Hagen, W. 1982, A&A, 114, 245
Tobin, J. J., Hartmann, L., Calvet, N., & D'Alessio, P. 2008, ApJ, 679, 1364
Tobin, J. J., Hartmann, L., Chiang, H.-F., et al. 2012, Natur, 492, 83
Tobin, J. J., Hartmann, L., Chiang, H.-F., et al. 2013, ApJ, 771, 48
Tobin, J. J., Kratter, K. M., Persson, M. V., et al. 2016a, Natur, 538, 483
Tobin, J. J., Looney, L. W., Li, Z.-Y., et al. 2016b, ApJ, 818, 73
Tobin, J. J., Looney, L. W., Wilner, D. J., et al. 2015, ApJ, 805, 125
Tobin, J. J., Sheehan, P. D., Megeath, S. T., et al. 2020, ApJ, 890, 130
Tychoniec, Ł., Manara, C. F., Rosotti, G. P., et al. 2020, A&A, 640, A19
Tychoniec, Ł., Tobin, J. J., Karska, A., et al. 2018, ApJS, 238, 19
Ulrich, R. K. 1976, ApJ, 210, 377
van Gelder, M. L., Tabone, B., Tychoniec, L., et al. 2020, A&A, 639, 87
van 't Hoff, M. 2019, PhD thesis, Leiden Univ.
van 't Hoff, M. L. R., Tobin, J. J., Harsono, D., & van Dishoeck, E. F. 2018a, A&A, 615, A83
van 't Hoff, M. L. R., Tobin, J. J., Trapman, L., et al. 2018b, ApJL, 864, L23
van 't Hoff, M. L. R., van Dishoeck, E. F., Jørgensen, J. K., & Calcutt, H. 2020, A&A, 633, A7
van 't Hoff, M. L. R., Walsh, C., Kama, M., Facchini, S., & van Dishoeck, E. F. 2017, A&A, 599, A101
van Zadelhoff, G.-J., van Dishoeck, E. F., Thi, W.-F., & Blake, G. A. 2001, A&A, 377, 566
Visser, R., Doty, S. D., & van Dishoeck, E. F. 2011, A&A, 534, A132
Visser, R., Kristensen, L. E., Bruderer, S., et al. 2012, A&A, 537, A55
Visser, R., van Dishoeck, E. F., Doty, S. D., & Dullemond, C. P. 2009, A&A, 495, 881
Vorobyov, E. I. 2009, ApJ, 704, 715
Walsh, C., Loomis, R. A., Öberg, K. I., et al. 2016, ApJL, 823, L10
Walsh, C., Millar, T. J., Nomura, H., et al. 2014, A&A, 563, A33
Walsh, C., Nomura, H., & van Dishoeck, E. 2015, A&A, 582, A88
Watanabe, N., & Kouchi, A. 2002, ApJL, 571, L173
Whitney, B. A., Wood, K., Bjorkman, J. E., & Wolff, M. J. 2003, ApJ, 591, 1049
Willacy, K., & Woods, P. M. 2009, ApJ, 703, 479

Williams, J. P., Cieza, L., Hales, A., et al. 2019, ApJL, 875, L9
Wilson, T. L., & Rood, R. 1994, ARA&A, 32, 191
Wolf, S., Padgett, D. L., & Stapelfeldt, K. R. 2003, ApJ, 588, 373
Xu, R., Bai, X.-N., & Öberg, K. 2017, ApJ, 835, 162
Yen, H.-W., Koch, P. M., Takakuwa, S., et al. 2017, ApJ, 834, 178
Yen, H.-W., Takakuwa, S., Ohashi, N., et al. 2014, ApJ, 793, 1
Yen, H.-W., Takakuwa, S., Ohashi, N., & Ho, P. T. P. 2013, ApJ, 772, 22
Yıldız, U. A., Kristensen, L. E., van Dishoeck, E. F., et al. 2015, A&A, 576, A109
Zhang, K., Bergin, E. A., Blake, G. A., Cleeves, L. I., & Schwarz, K. R. 2017, NatAs, 1, 0130
Zhang, K., Schwarz, K. R., & Bergin, E. A. 2020, ApJL, 891, L17